Monte Carlo Optimization of a Metal/Amorphous-Selenium Portal Imager

Martin Lachaîne

Medical Physics Unit
McGill University, Montreal
May, 1997

A thesis submitted to the Faculty of Graduate Studies and Research in partial fulfillment of the requirements for the degree of Master of Science

Abstract

An amorphous-Selenium (a-Se) based portal detector, which uses the metal substrate as a conversion plate, is studied using Monte Carlo techniques. The optimal thickness and material of the metal plate and a-Se thicknesses are investigated by modelling dose deposition in the a-Se layer for a 6 MV exit beam. Simulations of Detective Quantum Efficiency$DQE(f)$ show that although $DQE(0)$ increases with metal thickness up to d_{max}, there is a cross-over near 1 cycle/mm which indicates that smaller metal thicknesses are more useful to visualize edges and small objects. A similar cross-over, though not as prominent, is also observed with constant metal thickness while varying a-Se thickness. Tungsten front plates are shown be optimal in terms of DQE for the plates under investigation. The effect of the scattered beam, described by the Scatter Fraction SF and Scatter-to-Primary Ratio SPR, is also modelled to ensure that the front-plate, which also acts as a scatter-rejection tool, satisfactorily filters out the scatter component. The SF is measured experimentally with a prototype imager for four metal plate/a-Se combinations and agrees with the Monte Carlo results within experimental uncertainties.

Résumé

Un système d'acquisition numérique d'images pour la radiothérapie est étudié. Le détecteur consiste en une couche de sélénium amorphe (a-Se) déposée sur la surface arrière d'une plaque de métal qui sert à convertir les rayons-x en électrons. L'énergie absorbée dans la couche de a-Se, pour des photons ayant une énergie de 6 MV à leur sortie du patient, est simulée par des méthodes Monte Carlo afin de déterminer l'épaisseur et la composition optimale de la plaque de métal. Les valeurs de $DQE(f)$ découlant de ces simulations indiquent que même si $DQE(0)$ augmente avec l'épaisseur du métal jusqu'à une épaisseur de d_{max}, des plaques plus minces permettent mieux la visualisation des fréquences spatiales au-delà de 1 cycle/mm. Ce même effet, à un degré moindre, est observé avec la variation de l'épaisseur de la couche de a-Se. Les plaques de Tungsten ont les meilleurs DQE parmi les métaux étudiés. L'effet des photons diffusés sur la qualité des images, qui est décrit par les quantités SF et SPR, est simulé pour assurer une épaisseur suffisante de la plaque de métal pour filtrer ces photons diffusés et les électrons provenant du patient. Le SF est aussi mesuré expérimentalement pour quatre combinaisons de métal/a-Se; les résultats concordent avec ceux des simulations Monte Carlo.

Acknowledgments

I would like to thank my supervisor, Dr B. G. Fallone, for his guidance and encouragement throughout the completion of this work. His insight and resourcefulness have been of incalculable help. I am also grateful for the financial support which he has provided.

I am indebted to the entire Medical Physics department at McGill University, especially the director, Dr E. B. Podgorsak, for the strong background and education I have received in the past two years.

I greatly appreciate the help of my collegues, Tony Falco and Dimitre Hristov, for very useful discussions, and Corey Zankowski for his help in teaching me the EGS4 Monte Carlo code.

I cannot begin to thank my parents, André and Carole Lachaîne, my brothers Alexis and Pierre-André, and my grandmother Lucille Mayer for their continual love and support.

This thesis is dedicated to my love, Carey Satin, whose caring and commitment has kept me going through both good times and bad.

Table of Contents

List of Figures

Chapter 1: Introduction

1.1 Portal Imaging

In the treatment of cancer with radiation, the goal is to maximize the absorbed dose to the treatment volume while minimizing the dose to healthy tissues. To obtain an adequate dose distribution, diagnostic information is gathered and subsequently used to determine an appropriate treatment plan. In the transition from the plan to the actual radiation delivery, the errors which occur can be simplified by dividing them into two basic categories: errors in the magnitude of the dose delivered, and errors in positioning.[1] The former can be checked by using thermoluminiscent dosimeters (TLDs) on the entrance and exit side of the patient. The positioning errors, however, can only be checked with a two-dimensional image taken on the exit side of a patient. This practice is known as portal imaging, and was first reported in 1951 by Hare *et al*[2] who used film for supervoltage rotational therapy verification. With the advent of megavoltage treatment

beams, such as those generated by Cobalt-60 units and medical linear accelerators, films with higher sensitivity were designed for use in high-energy portal imaging.[3–5] There has also been extensive research aimed at the direct calculation of exit doses with portal imagers which is then compared to that expected from the treatment plan. This procedure could eventually replace TLDs for the verification of dose delivery.[6, 7]

The extraction of an image from a megavoltage photon beam has inherent problems. In this energy range, the Compton effect predominates in the patient, resulting in small differential attenuation coefficients within the patient anatomy and therefore low contrast. Also, a large amount of scattered photons and electrons reach the receptor which degrades contrast even further. To increase the sensitivity of the portal film imager, to shield from scattered electrons originating from the patient and to preferentially attenuate scattered photons also originating from the patient, a metal plate is often placed directly above the portal film. Droege and Bjarngard[8] have shown that the metal plate improves contrast by reducing the scattered radiation reaching the film. This metal plate is often referred to as a conversion plate, or build-up plate, since the photons transfer energy to electrons in the plate, which subsequently expose the film. Due to interactions in the conversion plate, there is a spreading out of the information, which results in a blurring effect on the image quality. Also, due to the randomness of interactions in the plate, additional noise is introduced to the image. Studies have been performed on these effects for various

metal/film combinations.[9–13]

Due to the low intrinsic contrast present in megavoltage imaging, it is desirable to use contrast-enhancing algorithms.[14–16] Since noise is magnified with the use of these algorithms, it is important to have an imaging process with a high signal-to-noise ratio.

Work has been done by digitizing film and manipulating the digital data with the aid of computers. Due to the time delay in both film development and subsequent digitization, the need for an inherently electronic portal imager is clear. Commercial electronic portal imaging devices (EPIDs) have become available, and others are presently in the research stage.

1.2 Electronic Portal Imaging Devices (EPIDs)

Boyer *et al*[17] provide an extensive review of EPIDs. Commercial EPIDs can be broken down into two basic categories: those based on the scanning liquid ionization chamber (SLIC),[18, 19] and fluoroscopic systems.[6, 20–22] SLIC systems are based on the principle of the ionization chamber, except the sensitive volume is filled with iso-octane liquid instead of air. Although the whole panel is filled with this liquid, the collection potential is only applied over one area (1.27×1.27 mm^2) at any given moment, and the resulting current is sampled. This is accomplished by the use of two parallel circuit boards, with each line being read off sequentially in a raster fashion. This results in low spatial resolution due to the pixel size.

To increase the dose absorbed in the liquid, a metal build-up plate is used as with film; the PortalVision system, by Varian Oncology Systems, uses a 1 mm steel plate for this purpose. The imager is placed on the exit side of the patient, and read-out is performed during irradiation. Although collection efficiency is high, only one area is read out at any given time, which results in loss of information elsewhere on the imager. This problem is partially solved, however, due to slow moving positive ions in the iso-octane liquid. A state of equilibrium is reached where the ions produced by the radiation are balanced by recombination. The dose required to obtain a useful image is however still quite large, on the order of 20–50 cGy.

Most other commercial portal imagers are based on fluoroscopy. The detector is phosphor, usually gadolinium oxysulfide (Gd_2O_2S), bound to a metal conversion plate. The incident high-energy photons mostly transfer their energy to electrons in the plate, which subsequently deposit their energy in the phosphor. This energy is converted into light photons, which are then reflected by a mirror, detected by a video camcera and turned into an digital signal by means of an analog-to-digital converter (frame grabber). The imaging process can be broken down into three steps:

i) Energy absorption, which will affect the resolution due to scattering in the detector, and the signal-to-noise properties

ii) Light production and transport within the phosphor, which will further reduce res-

olution and increase noise

iii) Collection of light and conversion to digital signal

In this system, the entire detector is active simultaneously, unlike the SLIC system which only collects signal in one region at any given time. However, the mirror/lens system has low light collection efficiency, on the order of 0.05%[23]. A number of frames must be added in a buffer to collect enough statistics to reduce noise. This results in an increase in patient dose. Images have been obtained with patient doses ranging from 0.5–7 cGy.[24]

Perhaps the most promising solution to this final step in the imaging chain comes from amorphous-Silicon (a-Si) based systems,[25, 26] which are currently in the research stage. These systems would couple the metal/phosphor detector to a matrix of photodiode-field effect transistors (FETs) made of hydrogenated amorphous silicon. The light produced in the phosphor creates electron-hole pairs in the photodiodes, which are subsequently stored in the photodiode capacitance. This stored charge is read out, one row at a time, by changing the line voltage which opens the FET gates. Signals are thus sent through the FETs onto DATA lines, and digitized to form an image. This collection method increases the light collection efficiency from approximately 0.05% to 50%, and holds promise for the future.

1.3 Amorphous Selenium Imager

Amorphous Selenium (a-Se), historically used for optical imaging,[27] was introduced into the medical imaging field in the 1950s by Schaffert.[28] A diagnostic imaging modality called xeroradiography in which a-Se was the detector was developed. The a-Se was attached to a metal aluminum substrate, and its surface was initially charged by corona charging. X-rays, modulated by a patient, absorb their energy in the a-Se layer, creating electron-hole pairs, which subsequently migrate in the electric field and neutralize the surface charge. This would result in a latent image represented by the surface charge distribution, corresponding to the incident x-ray distribution. In xeroradiography, the image was recorded by applying charged toner particles to the a-Se surface, which distributed themselves according to the field lines. A hard copy could then be obtained by pressing special coated paper over the attached toner particles.[29]

Xeroradiography gained interest in the field of mammography and in the imaging of extremities, but its use has declined partly due to a lower sensitivity than that of film. Lately, however, with novel methods to read out the surface charge distribution digitally, such as photoinduced discharge with a laser (PID),[30–33] and thin-film transistors (TFTs),[34] research into a-Se imagers has been revitalized.

In 1973, Wolfe *et al*[35] reported an a-Se based portal imager which used xeroradiographic toner to extract the latent image. In this system, the metal plate on which a-Se

is deposited faces away from the treatment beam. The detection efficiency of a-Se, however, is low at megavoltage energies. As with other portal imagers, a metal build-up layer would increase the dose absorbed in the a-Se, which would increase detector sensitivity. Our laboratory has investigated the use of a-Se for megavoltage portal imaging with the metal plate on which a-Se is deposited facing the x-ray beam.[36–41] A rudimentary method of measuring the surface voltage with a coupled electrostatic probe was used to study the imaging prospects of the system in our laboratory.

The main advantage of a-Se systems over phosphor-based systems is that image degradation due to light transport within the phosphor itself is avoided. The electron-hole pairs migrate to the surface within an electric field, resulting in less dispersion than that which exists in the conversion of x-rays to light and subsequent optical coupling processes. The energy exchange from x-ray absorption to light to an electronic image is reduced to an exhange from x-ray absorption directly into an electronic image. The optimal readout method for metal/a-Se systems is not clear, however, and is under investigation.

1.4 Thesis Motivation and Organization

All the portal imagers discussed above have a metal conversion plate facing the radiation beam. Work has been done by various authors on the optimal thickness for this front plate by considerations of the Detective Quantum Efficiency (DQE) and contrast enhancement by scatter rejection.

Jaffray *et al*[42] have studied the zero-frequency Detective Quantum Efficiency $DQE(0)$, and Radcliffe *et al*[43] the signal-to-noise ratio, due to dose deposition in a metal plate/phosphor imager using Monte Carlo techniques. Jaffray *et al* have also determined the effect of scatter on selected portal imagers by integrating primary and scatter fluence over detector response.[44] Although the image formation process with phosphor is very different to that of a-Se systems, the dose deposition can be modelled in a similar fashion. Our laboratory has previously performed preliminary studies of $DQE(f)$ for an a-Se detector for various metal plate/a-Se combinations for monoenergetic photon energies.[45]

In practice, a patient is placed between the source and the detector which both hardens the primary spectrum and produces scattered photons and electrons which also reach the detector. The goal of this work is to optimize, by Monte Carlo techniques, the metal plate thickness with a-Se for a 6 MV linear accelerator beam by taking both the hardened primary beam spectrum and the scattered beam into account. Verification of scattered

beam simulations are performed with the use of a scanning voltage probe system.

The organization of the thesis is as follows.

Chapter 2 gives background on the interaction of x-rays with the metal/a-Se imager and an outline of the EGS4 code with which these interactions are simulated. Some properties of amorphous Selenium are also discussed. The theories of Modulation Transfer Functions, Detective Quantum Efficiency and the effect of scatter on image quality are described. Chapter 3 outlines our Monte Carlo procedures for the determination of MTF, DQE, SF and SPR, and the experimental procedure followed for the measurement of SF. Chapter 4 discusses our results, with conclusions presented in Chapter 5.

References

1 Edited by T. R. Mackie and J. R. Palta, editors. *Teletherapy: Present and Future.* Proceedings of the 1996 Summer School. 1996.

2 H. F. Hare, J. Hale, and E. P. Pendergrass. Physical and clinical aspects of supervoltage rotational therapy. *Radiology*, 57:157, 1951.

3 R. W. Swain and R. J. Steckel. Beam localization in cobalt and megavoltage therapy during treatment. *Radiology*, 86:529, 1966.

4 A. Haus, S. Pinsky, and J. Marks. A technique for imaging patient treatment area during a therapeutic radiation exposure. *Radiology*, 97:653–656, 1970.

5 A. Haus, J. Marks, and M. Griem. Evaluation of an automatic rapid-processable film for imaging during the complete radio-therapeutic exposure. *Radiology*, 107:697–698, 1973.

6 J. Leong. Use of digital fluoroscopy as an on-line verification device in radiation therapy. *Phys. Med. Biol.*, 31:985–992, 1986.

7 M. C. Kirby and P. C. Williams. Measurement possibilities using an electronic portal imaging device. *Radiother. Oncol.*, 29:237–243, 1993.

8 R. T. Droege and B. E. Bjarngard. Influence of metal screens on contrast in megavoltage x-ray imaging. *Med. Phys*, 6:487–493, 1979.

[9] R. T. Droege and B. E. Bjängard. Metal screen-film detector MTF at megavoltage x-ray energies. *Med. Phys.*, 6(6):515–518, 1979.

[10] R. T. Droege. A megavoltage MTF measurement technique for metal screen-film detectors. *Med. Phys.*, 6(4):272–279, 1979.

[11] P. Munro, J. A. Rawlinson, and A. Fenster. Therapy imaging: a signal-to-noise analysis of metal plate/film detectors. *Med. Phys.*, 14:975–984, 1987.

[12] T. Falco and B. G. Fallone. Characteristics of metal-plate/film detectors at therapy energies: Part 1 (MTF). *submitted to Med. Phys.*, 1997.

[13] T. Falco and B. G. Fallone. Characteristics of metal-plate/film detectors at therapy energies: Part 2 (DQE). *submitted to Med. Phys.*, 1997.

[14] G. Sherouse, J. Rosenamn, H. McMurr, S. Pizer, and E. Chaney. Automatic degital contrast enhancement of radiographic portal films. *Int. J. Radiat. Oncol. Biol. Phys.*, 13:801–806, 1987.

[15] S. M. Pizer, E. P.. Amburn, J. D. Austin, R. Cromartie, A. Geselowitz, T. Greer, B. Ter Haar Romeny, J. B. Zimmerman, and K. Zuiderveld. Adaptice vistogram equalization and its variations. *Comput. Vision, Graphics, and Image Processing*, 39:355–368, 1987.

[16] I. Crooks and B. G. Fallone. Contrast enhancement of portal images by selective histogram equalization. *Med. Phys.*, 20:199–204, 1993.

[17] A. L. Boyer, L. Antonuk, A. Fenster, M. van Herk, H. Meertens, P. Munro, L. Reinstein, and J. Wong. A review of electronic portal imaging devices (EPIDs). *Med. Phys.*, 19:1–16, 1992.

[18] M. Van Herk and H. Meertens. A matrix ionization chamber imaging device for on-line patient setup verification during radiotherapy. *Radiother. Oncol.*, 11:369–378, 1988.

[19] M. Van Herk and H. Meertens. A digital imaging system for portal verification. *Proceedings of the 9th International Conference on the Use of Computers in Radiation Therapy*, pages 371–374, 1987.

[20] S. Shalev, T. Lee, K. Lesczcynski, S. Cosby, and T. Chu. Video techniques for on-line portal imaging. *Computerized Medical Imaging and Graphics*, 13:217–226, 1989.

[21] A. G. Visser, H. Huizenga, V. G. M. Althof, and B. N. Swanenburg. Performance of a prototype fluoroscopic radiotherapy imaging system. *Int. J. Radiati. Oncol. Biol. Phys.*, 18:43–50, 1990.

[22] P. Munro, J. A. Rawlinson, and A. Fenster. A digital fluoroscopic imaging device for radiotherapy localization. *Proceedings of SPIE*, 321–329:1090, 1989.

[23] L. E.. Antonuk, J. Boudry, W. Huang, D. L. McShan, E. J. Morton, J. Yorkston, M. J. Longo, and R. Street. Demonstration of megavoltage and diagnostic x-ray imaging with hydrogenated amorphous silicon arrays. *Med. Phys.*, 19:1455–1465, 1992.

[24] S. Webb. *The Physics of Three-Dimensional Radiation Therapy*. IOP Publishing Ltd, 1993.

[25] L. E. Antonuk, J. Yorkston, J. Boudry, M. Longo, and R. A. Street. Large area amorphous silicon photodiode arrays for radiotherapy and diagnostic imaging. *Nuclear Instrumentation and Method*, A310:460–464, 1989.

[26] L. E. Antonuk, J. Yorkston, J. Boudry, M. Longo, J. Jimenez, and R. A. Street. Development of hydrogenated amorphous silicon sensors for high energy photon radiotherapy imaging. *IEEE Transactions of Nuclear Science*, NS-37(2):165–170, 1990.

[27] C. F. Carlson. U.S. Patent 221776. 1938;1940.

[28] R. Schaffert. U.S. Patent 2666144. 1950;1954.

[29] J. W. Boag. Xeroradiography (review). *Phys. Med. Biol.*, 18:3–37, 1973.

[30] A. Zermeno, T. Kirby, R. Cowart, L. Marsh, and P. Ong. Laser readout of electrostatic images. *Application of Optical Instrumentation to Medicine VII, Proceedings of SPIE*, 173:81–87, 1979.

[31] E.L. Cook, J. D. Edwards, O. L. Nelson, and J. E. Potts. Performance of a high resolution radiographic detector. *The society of imaging science and technology 47th annual conference ICPS*, page 699, 1994.

[32] J. A. Rowlands and D. M. Hunter. X-ray imaging using amorphous selenium:

Photoinduced discharge (PID) readout for digital general radiography. *Med. Phys.*, 22:1983–2005, 1995.

[33] J. A. Rowlands and J. E. Taylor. Design of a laser scanner for a digital mammography system. *Med. Phys.*, 23:755–758, 1996.

[34] W. Zhao and J. A. Rowlands. X-ray imaging using amorphous selenium: feasibility of a flat panel self-scanned detector for digital radiology. *Med. Phys.*, 22:1595–1604, 1995.

[35] L. Wolfe, L. Kalisher, and B. Considine. Cobalt-60 treatment field verification by xeroradiography. *A. J. R.*, 18:3–37, 1973.

[36] B. G. Fallone and T. Falco. Megavoltage imaging method using a combination of a photoreceptor with a high energy photon converter and intensifier. *Reg. # 625063, U.S. Patent to be released in August*, 1997.

[37] T. Falco and B. G. Fallone. Portal imaging: Comparing metal-plate film and electrostatic-based detectors. *Med. Phys. (Abstract)*, 23:797, 1996.

[38] H. Wang, T. Falco, and B. G. Fallone. A metal screen-amorphous selenium based image receptor in megavoltage portal imaging. *Med. Phys. (Abstract)*, 23:1130, 1996.

[39] B. G. Fallone, T. Falco, H. Wang, and N. Araj. An electrostatic-based detector for portal imaging. *4th International Workshop on Electronic Portal Imaging, Abstract Proceedings, Edited by M. Van Herk and K. Gilhuijs, Amsterdam*, pages 64–65, 1996.

[40] T. Falco and B. G. Fallone. Portal imaging: comparing metal-plate/film with electrostatic-based detectors. *Proceedings of 42nd annual Canadian Organization of Medical Physicists Conference*, pages 56–59, 1996.

[41] H. Wang and B. G. Fallone. Monte Carlo calculations of the MTF and DQE of a Cu/a-Se image receptor in megavoltage portal imaging. *Proceedings of 42nd annual Canadian Organization of Medical Physicists Conference*, pages 286–289, 1996.

[42] D. A. Jaffray, J. J. Battista, A. Fenster, and P. Munro. Monte Carlo studies of x-ray energy absorption and quantum noise in megavoltage transmission radiography. *Med. Phys.*, 22:1077–1088, 1995.

[43] T. Radcliffe, G. Barnea, B. Wowk, R. Rajapakshe, and S. Shalev. Monte Carlo optimization of metal/phosphor screens at megavoltage energies. *Med. Phys.*, 20:1161–1169, 1993.

[44] D. A. Jaffray, J. J. Battista, A. Fenster, and P. Munro. X-ray scatter in megavoltage transmission radiography: Physical characteristics and influence on image quality. *Med. Phys.*, 21:45–60, 1994.

[45] H. Wang, B. G. Fallone, and T. Falco. Monte Carlo simulations of a metal/a-Se portal detector. *Radiol. Oncol*, 30:291–297, 1996.

Chapter 2: Theory

2.1 The Interaction of X-rays with the Metal/a-Se Detector

An x-ray photon impinging on matter will interact in a series of stochastic energy transfer processes. In the megavoltage energy range, the three most commonly occuring processes are the photoelectric effect, Compton effect and pair production. The probability of occurence of each process is given by its cross-section, which depends on the photon's energy, the material's density ρ and its atomic number Z.[1]

The photon will lose some or all of its energy by either transferring its energy to electrons, or in creating electron-positron pairs. These secondary charged particles will subsequently interact with the medium, losing energy by collisional and radiative processes. Electrons interacting with atomic nuclei will result in the emission of bremsstrahlung photons, which will continue the chain of interactions.

Secondary charged particles, as they suffer collisional interactions in the medium, deposit their energy in the medium resulting in *absorbed dose*, which is defined as the energy absorbed locally in the medium per unit mass.

Consider a photon beam impinging perpendicularly on a semi–infinite slab. The photons will transfer their energy to electrons, which are primarily forward-scattered at megavoltage energies, resulting in energy being deposited on average deeper in the slab. Therefore, as the depth increases from zero, the dose will increase due to a build-up of electrons above the point in question. This will occur until a depth near the average electron range. The dose will then begin to decrease due to the attenuation of photons. This distribution, normalized to 100 at the depth of maximum dose d_{max}, is commonly called the Percent Depth Dose (PDD) in radiation dosimetry. The depth d_{max} in water is approximately 1.5 cm for a 6 MV beam, and increases with energy. Since for megavoltage energies the Compton effect dominates, and the Compton cross-section varies little with atomic number and linearly with density, for materials other than water a good approximation for d_{max} is to scale the value for water by the material's density.

In the metal/a-Se imager, as with other x-ray imagers, the sensitive region is basically a detector of absorbed energy. Modelling the energy deposition in the a-Se layer is thus very useful in studying the detector properties. The primary purpose for the presence of a front metal plate is to allow electron build-up. For this reason, it seems intuitive that

a thickness d_{max} is ideal. However, there are other aspects of the plate to consider.

Due to the stochastic nature of x-ray energy deposition, noise is introduced into the process. Therefore although the signal is increased by the plate, its effect on the *signal-to-noise ratio* must be examined. Also, interactions within the metal plate will cause a blurring of the image, which is expected to increase with plate thickness.

In portal imaging, a patient lies between the x-ray source and the receptor. For the case of a linear accelerator, for which portal imaging is most commonly used, the x-rays incident on the patient have a continuous spectrum of energies. Upon traversing the patient, lower-energy photons will be preferentially removed. The primary beam spectrum on the exit side will thus have a higher average energy, resulting in *beam hardening*. Also, scattered photons and electrons originating from the patient will interact with the detector. Another role of the front plate is to preferentially attenuate the lower-energy scattered photons, and decrease the electron scatter.

The concepts of signal-to-noise ratio, blur and the effect of scatter will be discussed in greater detail in Section 2.4

2.2 The Physics of a-Se

Selenium (atomic number Z=34) is usually found in a crystalline state. The amorphous state is formed by controlled evaporation of the Selenium and even deposition onto a metallic substrate. By this method, a-Se can be shaped into a large-area, flat-panel detector.

Selenium is a semi-conductor with a band-gap of 2.3 eV.[2] It has the property of being a photoconductor, and thus exhibits greatly enhanced conductivity when irradiated with electromagnetic energy (e.g. visible or x-ray photons).

The energy of photons impinging is used to create electron-hole pairs. If optical photons are used to irradiate the a-Se, most will deposit all of their energy in a small layer at the surface. If higher energy photons, such as x-ray photons, are used, only a fraction of their energy may be absorbed in the a-Se layer. In either case, the average number of electron-hole pairs n_c produced is proportional to the absorbed energy E_{abs} and is given by

$$n_c = \frac{E_{abs}}{W_o} \tag{2.1}$$

where W_o is the average energy needed to create one electron-hole pair. A simple formula derived by Klein,[3] which has been shown to agree with a large number of semiconductors,[4] predicts W_o has a value of approximately 7 eV.

When a uniform positive charge is distributed on the a-Se surface, for example by corona charging, an electric field will be set up within the a-Se. When the surface is then irradiated, with a position-dependent intensity distribution, electron-hole pairs will be produced, the amount proportional to the incident intensity distribution as seen by Eq. (2.1). In the presence of the electric field, these electron-hole pairs will migrate to opposite surfaces of the a-Se. The negative electrons will be attracted to the uniform positive charge, and will partially neutralize it. A surface charge will thus result which will reflect the original intensity distribution.

Although the number of electron-hole pairs generated are given by n_c, a fraction of these will recombine before reaching the a-Se surface. The mechanism of recombination is not well understood, but depends on the electric field and possibly the energy.[5] The average number of electron-hole pairs which reach the surface before recombining, n, is given by

$$n = \frac{E_{abs}}{W} \tag{2.2}$$

where W is the energy absorbed per electron-hole pair which reaches the a-Se surface and has a value of about 50 eV of absorbed energy for an electric field of 10 V/μm.[6] The relationship between W and W_o is given by

$$W = \frac{W_o}{\eta} \tag{2.3}$$

where the photogeneration efficiency η is the fraction of created electron-hole pairs which do not reach the surface.

In the past, there have been no convincing experiments showing a variation of W with photon energy for kilovoltage x-rays[5], but a recent study has found the following variation[7]

$$W = \begin{cases} 20\,eV & if\ E_i < 10\,keV \\ 40\,eV & if\ 10\,keV < E_i < 50\,keV \\ 60\,eV & if\ E_i > 50\,keV \end{cases} \quad . \tag{2.4}$$

However, even with such a variation it is likely that an average over energy, $\overline{W}$, will remain a good approximation. For this reason, it is important to study the x-ray energy absorption properties in a-Se. Also, since the primary role of the conversion plate is to change the distribution of energy absorbed, the optimal plate thickness can be determined by exploring its effect on energy deposition in the a-Se.

Although the physical process of energy absorption is the first step in the process of image formation, it is not directly measurable. However, plate voltage can be measured with an electrostatic probe, and a simple model can relate plate voltage to energy absorbed.[8]

In the dark, the a-Se layer acts somewhat like a capacitor. A uniform surface charge density σ will result in a surface voltage V given by

$$V = \frac{\sigma d}{\epsilon} \tag{2.5}$$

where d is the a-Se thickness and ϵ is its dielectric constant. If an infinitessimal amount of energy dE_{abs} is absorbed in the a-Se, this will result in dn electron-hole pairs which migrate to the a-Se surface, according to Eq. (2.2), and partially neutralize the surface charge by an amount

$$d\sigma = -\frac{e}{A}dn = -\frac{em}{A\overline{W}}dD \tag{2.6}$$

where e is the electron charge, A is the surface area, m is the mass of a-Se in which energy is deposited, and the notation has been changed to absorbed dose D, i.e. energy absorbed per unit mass.

It has been shown that $\overline{W}$ depends approximately on the electric field in the a-Se by

$$\overline{W} \approx C\left(\frac{V}{d}\right)^{-\frac{2}{3}} \tag{2.7}$$

where C is a constant of proportionality.[6] Combining Equations (2.5), (2.6) and (2.7), this leads to

$$dV = -\frac{em}{\epsilon AC}d^{\frac{1}{3}}V^{\frac{2}{3}}dD \quad . \tag{2.8}$$

Integrating and substituting the initial voltage V_o for dose $D = 0$, the equation relating surface voltage to absorbed dose becomes

$$V(D) = V_o\left(1 - \frac{\alpha d^{\frac{1}{3}}}{\epsilon V_o^{\frac{1}{3}}} \cdot D\right)^3 \tag{2.9}$$

where α is a constant which describes the sensitivity of a-Se to x-rays. According to this model, the voltage would drop to zero at a dose given by

$$D_m = \frac{\epsilon}{\alpha} \cdot \left(\frac{V}{d}\right)^{\frac{1}{3}} \quad , \tag{2.10}$$

which describes the characteristic range. This parametrization has been shown to fit the sensitivity curves experimentally.[8] The image contrast, according to this model, would then be given by the slope of the sensitivity curve, i.e.

$$\frac{dV}{dD} = -\frac{3\alpha d^{\frac{1}{3}} V_o^{\frac{2}{3}}}{\epsilon} \cdot \left(1 - \frac{D}{D_m}\right)^2 \quad . \tag{2.11}$$

From Eq. (2.9), there exists a definite non-linear relationship between absorbed energy and the measured plate voltage, analogous to an H&D curve with film. If desired, the final image can thus be converted to relative dose.

2.3 The EGS4 Monte Carlo Code System

2.3.1 Particle Transport in EGS4

EGS4 (Electron Gamma Shower) is a Monte Carlo computer code which simulates the interaction of photons and electrons in matter.[9] The energy range for which EGS4 can be validly used is from about 1 keV to several thousand GeV for photons, and approximately 10 keV to several thousand GeV for electrons or positrons. EGS4 has been tested extensively in the energy range of interest.[10]

Particle transport in EGS4 is based on the mean free path, λ, the average distance a particle will go before suffering an interaction. This distance will depend on the total molecular cross-section σ_t, which is proportional to the probability of interaction and is given by

$$\lambda = \frac{M}{N_a \rho \sigma_t} \tag{2.12}$$

where M is the molecular mass, N_a is Avogadro's number, and ρ is the material's density. The number of mean free paths traversed from x_o to x, N_λ, will be given by

$$N_\lambda = \int_{x_o}^{x} \frac{dx}{\lambda(x)} \quad . \tag{2.13}$$

This number is sampled with the help of a random number generator and is used to find the next location of interaction. The mean free path changes if either the particle enters a new medium or it loses energy.

Once the next location of interaction is determined, the specific type of interaction must be determined according to the individual interaction cross-sections, and the parameters associated with the relevant interaction (such as direction, energy transfer, etc) must be determined.

2.3.2 Photon Transport

For photons, the major interactions involved are Compton scattering, photoelecric scattering and pair production. Rayleigh (coherent) scattering may also be important

depending on the energy range in question. Photon interaction cross-sections are sufficiently small that particle transport can be approximated by assuming that photons travel in a straight line with constant energy between interactions. EGS4 thus samples N_λ, calculates λ, and calculates the distance $N_\lambda\lambda$. The particle is then transported by this distance, or to the boundary if the distance to the boundary is less than $N_\lambda\lambda$. If the particle enters a new medium, λ must be recalculated and proper bookkeeping performed. N_λ is then decremented by the proper amount according to the number of mean free paths traversed during the transport step. This process is repeated until N_λ reaches zero, at which point the particle will interact.

2.3.3 Charged Particle Transport

For charged particles, i.e. electrons and positrons, the most common interactions are elastic Coulomb scattering by nuclear potentials (Molière Scattering), inelastic scattering of atomic electrons (Møller or Bhabba scattering), positron annihilation and bremsstrahlung. Since the cross-sections become very large as the particle energy approaches zero, simulation at every interaction becomes impractical. The simulation of interactions are thus handled differently from photons.

To solve this problem, EGS4 defines cutoff energies, called AE for electrons and AP for photons (defined as total energy, i.e. including rest mass). Above these energies particle interactions are treated as discrete, and below them they are treated in a continuous

manner by grouping many interactions together. This is possible since a large amount of small momentum transfers occur in this case, which results in deviations from the average being small.

2.3.4 EGS4 User Codes

A block diagram of the EGS4 code is shown in Fig. 1. Users must perform two tasks to define their problem of interest within the EGS4 code. The first is to define the mediums used. This is done with the EGS4 preprocessor, called PEGS4, in which any element (from atomic numbers 1 through 100), mixture or compound can be defined. The user supplies parameters such as the density, cutoff values AE and AP, and energy range of interest, and PEGS4 subsequently calculates the relevant cross-sections to be used by EGS4. This data need only be generated once for each set of media used.

The rest of the problem is defined in the EGS4 *user code*. EGS4 is written in Mortran3, which is basically an extension to the FORTRAN programming language. The user code contains a MAIN program, and two subroutines: HOWFAR, which defines the geometry, and AUSGAB, which defines how quantities (such as fluence or dose) are scored.

The basic way in which communication with the EGS4 code is accomplished is through COMMON variables, i.e. variables which are shared between user-written code and the EGS4 code. These variables are initialized through the MAIN user program.

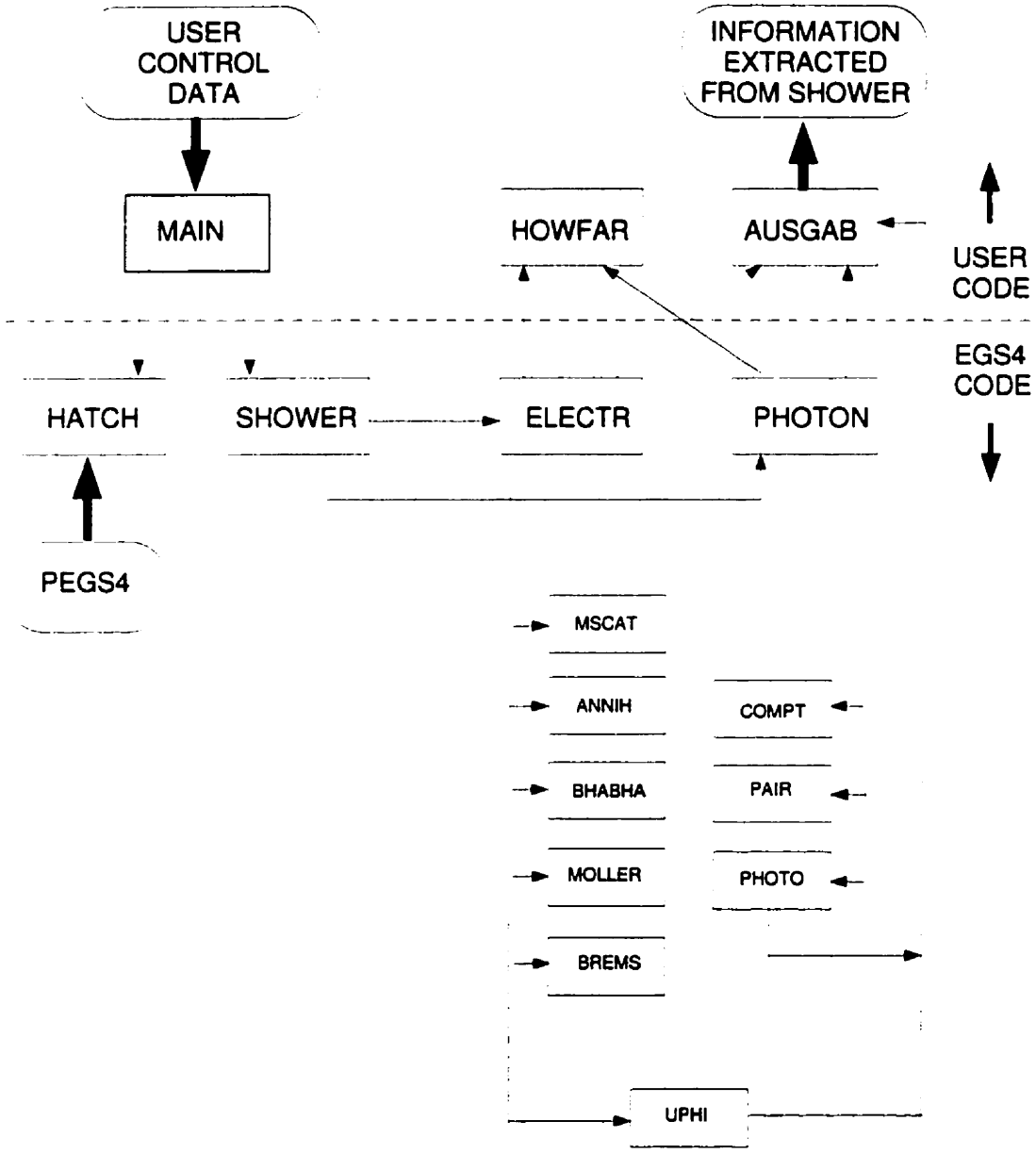

Figure 1: Block diagram of the EGS4 code structure (taken from Nelson *et al*[9])

The MAIN program must then call a subroutine called HATCH, which reads the data generated by PEGS4. The actual radiation transport is called by the SHOWER subroutine, which takes as input parameters such as the position (XIN, YIN, ZIN), direction cosines (UIN, VIN, WIN), energy (EIN) and charge (IQIN) of the incident particle. Thus if these parameters are not constant, for example if an energy spectrum is used or photons originate from a point source and therefore have different direction vectors, these parameters are sampled randomly from a probability distribution in the MAIN program. SHOWER thus generates a single shower history per call, and is generally called many times until sufficient statistics are acquired. Particles generated in the shower are kept in the stack, with the lowest energy particle being at the top of the stack. Particle histories are terminated when energy cut-off variables are reached. The cutoffs AP and AE can be over-ridden by defining photon and electron cutoffs PCUT and ECUT in the MAIN subroutine; these new cut-offs will be in effect only if they are larger than AP and AE. Raising cut-off values reduces computation time, possibly at the expense of accuracy. Their values must be given careful consideration.

The user-written subroutine HOWFAR defines the specific simulation geometry. This is done by writing code which finds the closest distance to boundaries and testing whether the particle should be transported to the boundary or undergo normal transport. This subroutine keeps account of which region the particle is in.

The second user-written subroutine, AUSGAB, defines the manner in which quantities are to be scored. This is done by determining whether a particle is in a particular sensitive region, and then calculating and scoring the required quantity. AUSGAB is called in the following cases:

i) A particle is about to be transported

ii) A particle is about to be discarded due to its energy being below the cut-off energies

iii) A particle is about to be discarded due to a user request from HOWFAR

iv) A photoelectric interaction has occured and either:

   a) the particle is about to be discarded due to its energy being below the K-edge binding energy, or

   b) a fluorescent photon is about to be discarded with the K-edge binding energy.

Each time AUSGAB is called, an appropriate parameter (IARG) is passed which indicates the reason for which it was called. An extension to these parameters is also possible if required, so that more specific situations can be analysed; for example, the number of times an in-flight positron annihilation occurs can be determined by counting the number of times AUSGAB is called with IARG=12.

Code can also be written in AUSGAB to keep track of specific particles and all of their progeny. This is done by using a variable called LATCH, whose value can be passed on by EGS4 to subsequently generated particles. For example, if one wants to

score dose originating only from photons undergoing Compton scattering, every time a Compton scattering event occurs (which can be determined with IARG), the LATCH variable (initialized to zero) can be incremented, which will be passed on to the particle's progeny. Dose can then be scored only if energy absorbed arises from particles with LATCH > 0.

As previously discussed, the number of electron steps per unit length is exceedingly large. The accuracy of the EGS4 model relies on the size of the electron steps; the smaller the steps the more accurate the model, at the expense of simulation time. An appropriate balance between accuracy and time is achieved by an algorithm introduced by Biejalew *et al*[11], called the parameter reduced electron-step algorithm (PRESTA). Far away from boundaries, larger steps are chosen, and the step size decreases close to the boundaries. The PRESTA algorithm can be incorporated into any user code, and saves computation time while automizing the selection of step sizes.

2.4 System Transfer Properties

Since the process of energy absorption is linear with input fluence (assuming enough statistics are collected), the theory of linear systems can be used to quantify the blur and signal-to-noise properties of the metal/a-Se detector.[12, 13] This section covers the basic theory of these properties, and also the effect of scatter on image quality.

2.4.1 Blur: The Modulation Transfer Function

The physics of the interaction of high energy photons with the electrostatic portal imager results in an intrinsic blur. To quantify this blur, it is useful to temporarily forget its underlying physical principles and to treat the imager as an input-output system. The input, which would in this case represent the incident x-ray fluence distribution, is represented mathematically as $I(x,y)$, and the output, which might be the final image distribution, is represented as $O(x,y)$. The role of the imager is to map the set of all possible inputs into a corresponding set of outputs, which can be represented mathematically as applying an operator S. The output will then be related to the input by

$$O(x,y) = S\{I(x,y)\} \tag{2.14}$$

The system response can be simplified if certain restrictions are imposed on the operator S. The first assumption made about the system is that of *linearity*. Mathematically, this implies that if inputs $I_1(x,y)$ and $I_2(x,y)$ produce outputs $O_1(x,y)$ and $O_2(x,y)$

respectively, then

$$S\{af_1(x,y) + bf_2(x,y)\} = aS\{f_1(x,y)\} + bS\{f_2(x,y)\} \tag{2.15}$$

where a and b are constants. This implies that if the input is broken down into a weighted sum of elementary inputs, the output will be a weighted sum of the outputs corresponding to these elementary inputs.

The second assumption is that of *shift invariance*. This implies that shifting an input function by (x', y') will merely shift the output function, but not change its shape. This implies mathematically that

$$O(x - x', y - y') = S\{I(x - x', y - y')\} \quad . \tag{2.16}$$

It is useful to consider a "point-like" input at coordinates (x', y'), which can be represented as a two-dimensional delta function $\delta(x - x', y - y')$. The corresponding output, denoted as $P(x, y; x', y')$, is referred to as the Point Spread Function (PSF). Since the system is assumed to be shift-invariant, the PSF must only depend on the differences $x - x'$ and $y - y'$, and is denoted by $P(x - x', y - y')$. Using the shifting property of the delta function, any input can be expressed as a sum of delta functions, implying that any output function is related to its corresponding input function by

$$O(x,y) = S\left\{ \int_{-\infty}^{\infty} \int_{-\infty}^{\infty} I(x',y')\delta(x - x', y - y')dx'dy' \right\} \quad . \tag{2.17}$$

The function can then be seen as a weighting function, analogous to the constants a and b in Equation (2.15). Using the linearity assumption, the operator S can thus be moved inside the integral so that it acts only on the delta function. Since the response of a delta-function input has been defined as the PSF, Equation (2.17) becomes

$$O(x,y) = \int_{-\infty}^{\infty}\int_{-\infty}^{\infty} I(x',y')P(x-x',y-y')dx'dy' \quad . \tag{2.18}$$

Equation (2.18) is a convolution integral, which can be represented in shorthand notation as

$$O(x,y) = I(x,y) \otimes P(x,y) \tag{2.19}$$

which shows that the role of the system is to transform the input function into an output function by convolving it with the Point Spread Function.

It is common practice to interpret the imaging properties of a system in the spatial frequency domain rather than in the position domain. The input function $\mathcal{I}(u,v)$ and output function $\mathcal{O}(u,v)$ as functions of spatial frequency are given by their Fourier Transforms,

$$\mathcal{I}(u,v) = \int_{-\infty}^{\infty}\int_{-\infty}^{\infty} I(x,y)e^{-2\pi i(ux+vy)}dxdy \tag{2.20}$$

$$\mathcal{O}(u,v) = \int_{-\infty}^{\infty}\int_{-\infty}^{\infty} O(x,y)e^{-2\pi i(ux+vy)}dxdy \tag{2.21}$$

where u and v are the x and y components of spatial frequency, respectively. Taking the Fourier Transform of Equation (2.18) and rearranging, it can be proven that the analog

to Equation (2.19) in the spatial frequency domain is

$$\mathcal{O}(u,v) = \mathcal{I}(u,v) \cdot \mathcal{P}(u,v) \tag{2.22}$$

where $\mathcal{P}(u,v)$ is the Fourier Transform of the Point Spread Function, i.e.

$$\mathcal{P}(u,v) = \int_{-\infty}^{\infty}\int_{-\infty}^{\infty} P(u,v)e^{-2\pi i(ux+vy)}dxdy \quad . \tag{2.23}$$

The role of the imaging system can thus be seen as a "spatial frequency filter". Since the Fourier Transform of a delta function is a constant, a perfect system transfers all spatial frequencies equally. Real systems, however, will usually degrade increasing spatial frequencies.

If the function $\mathcal{P}(u,v)$ were measured, it would provide a complete description of the system blur (provided the assumptions of linearity and shift-invariance on the system are valid). Conceivably, an infinitely thin, collimated beam of x-ray photons could be set up to impinge on the detector, and its measured response would be the PSF. In practice, however, using a point source would require a long exposure time to acquire an image; a line source, i.e. photons collimated by a long and narrow slit, is frequently used in its place. If a line source is parallel to the y-axis, a profile of the resulting distribution in the x-direction is called the Line Spread Function (LSF), given by

$$L(x) = \int_{-\infty}^{\infty} P(x,y')dy' \tag{2.24}$$

and can be seen as a one-dimensional projection of the PSF. It can be shown that if the PSF is real and isotropic, it can be completely specified by the LSF. The one-dimensional Fourier Transform of the LSF, $\mathcal{L}(u)$, given by

$$\mathcal{L}(u) = \int_{-\infty}^{\infty} L(x)e^{-2\pi iux}dx \tag{2.25}$$

would thus contain the same information as $\mathcal{P}(u,v)$. It can also be shown that if the LSF is real and even, then $\mathcal{L}(u)$ is real and thus can be specified by its magnitude. This leads to the quantity commonly used to measure blur, the Modulation Transfer Function (MTF), defined as

$$MTF(f) = \left|\frac{\mathcal{L}(f)}{\mathcal{L}(0)}\right| \tag{2.26}$$

where the notation for spatial frequency u has been changed to f since only one dimension is used. It contains the same information as $\mathcal{P}(u,v)$, as long as the assumptions mentioned previously hold, and thus fully describes the way in which the system degrades spatial frequencies.

When measuring a LSF, two main factors arise which depart from the ideal case. The first comes from the discrete sampling of the LSF. This can be expressed mathematically as the multiplication by a *comb* function of spacing Δx, given by

$$comb\left(\frac{x}{\Delta x}\right) = \sum_{n=-\infty}^{\infty} \delta(x - n\Delta x) \quad . \tag{2.27}$$

The second factor is that the x-ray beam used as a "line source" has a finite width w, given by

$$rect\left(\frac{x}{w}\right) = \begin{cases} 1 \; if \; |x| \leq \frac{w}{2} \\ 0 \; if \; |x| > \frac{w}{2} \end{cases} \quad . \tag{2.28}$$

The measured Line Spread Function, LSF_m, can thus be represented by

$$LSF_m(x) = LSF(x) \otimes rect\left(\frac{x}{w}\right) \cdot comb\left(\frac{x}{\Delta x}\right) \quad . \tag{2.29}$$

To find the resulting "measured" Modulation Transfer Function, MTF_m, the absolute value of the Fourier Transform of LSF_m must be taken (and normalized to unity at zero frequency), noting that in going from position to spatial frequency space, multiplications become convolutions (and vice-versa). The result is

$$MTF_m(f) = MTF(f) \cdot |sinc(w \cdot f) \otimes comb(\Delta x \cdot f)| \, , \tag{2.30}$$

where the $sinc$ function is defined as

$$sinc(\xi) = \frac{sin(\pi\xi)}{\pi\xi} \, . \tag{2.31}$$

The effect of the slit width on the measured MTF is thus to attenuate the real MTF by a $sinc$ function, which falls to zero at

$$f_{zero} = \frac{1}{w} \, . \tag{2.32}$$

If the oscillations in the $sinc$ function past this point are neglected, this means that the maximum spatial frequency which could possibly be of interest in the measured MTF

is f_{zero}. The effect of sampling, on the other hand, is to repeat the MTF at invervals $\frac{1}{\Delta x}$. This could cause a problem if two adjacent repetitions overlap; if the maximum frequency of interest is smaller than the so-called Nyquist frequency, given by

$$f_{max} = \frac{1}{2\Delta x}\,, \tag{2.33}$$

then this problem will be averted. Since the maximum frequency which could possibly be of interest is given by Eq. (2.33), this leads to the condition

$$w \geq 2 \cdot \Delta x \tag{2.34}$$

i.e. the sample spacing must be less than half the width of the slit.

Once Equation (2.34) is satisfied, the attenuation of the measured MTF by the $sinc$ function must be corrected for. Ideally, one could divide out the $sinc$ function, but this would lead to increasing errors as the $sinc$ function dropped off to zero. For this reason it must be ensured that f_{zero}, which is determined by the slit width w via Equation (2.32), is much greater than the maximum spatial of frequency of interest to be studied, f_{int}. The slit width is therefore limited by two quantities, Δx and f_{int}, by the relation

$$2 \cdot \Delta x \leq w << \frac{1}{f_{int}}\quad . \tag{2.35}$$

In portal imaging, most objects of clinical interest are large, on the order of 1 cm.[14] Spatial frequencies below 1 cycle/mm are important for the visualization of low contrast anatomical features; however, higher spatial frequencies may be useful in the visualization

of these low-contrast edges. It is unlikely, however, that any spatial frequencies much higher than 10 cycles/mm would be of any clinical use; for this reason, f_{int} was set to 10 cycles/mm in this work.

2.4.2 Detective Quantum Efficiency

X-ray photons impinging on the portal imager interact with the metal plate and a-Se layer, producing high energy electrons. These electrons may or may not deposit part of their energy in the a-Se layer, producing a measurable signal. The fraction of incident photons which lead to the deposition of energy in the a-Se layer is called the Quantum Absorption Efficiency, η.

Due to the statistical nature of the interaction of x-rays with matter, the energy deposited in the a-Se layer is variable thus introducing noise to the system response. In imaging, the signal and noise properties of a system are usually characterized by a quantity known as the Detective Quantum Efficiency (DQE), defined as

$$DQE = \left(\frac{SNR_{out}}{SNR_{in}}\right)^2 \tag{2.36}$$

where SNR_{in} and SNR_{out} are the input and output signal-to-noise ratios, respectively.

Consider N_{in} monoenergetic photons of energy E_i impinging on the detector. If the noise in this incident distribution is assumed to be Poissonian, then it is given by

$\sqrt{N_{in}}$, which leads to

$$SNR_{in} = \sqrt{N_{in}} \quad . \tag{2.37}$$

As described above, $N = \eta N_{in}$ photons will deposit energy in the sensitive region and cause a measurable pulse. Of these photons, $n(E, E_i)$ will deposit energy between E and $E + dE$ per unit energy interval. Since the "signal" is proportional to the energy deposited, the signal dS from the pulses between E and $E + dE$ is given by $dS(E) = n(E, E_i)EdE$. Assuming a Poisson distribution, the variance originating from pulses between E and $E+dE$ is given by $d\sigma_S^2 = n(E, E_i)E^2dE$, where σ_s is the standard deviation. Integrating the signal and noise over energy and substituting into Eq. (2.36), the DQE will thus be given by

$$DQE = \left(\frac{1}{\sqrt{N_{in}}} \cdot \frac{\int dS}{\sqrt{\int d\sigma_S^2}} \right)^2 = \frac{\left(\int_0^\infty \frac{n(E,E_i)}{N_{in}} EdE \right)^2}{\int_0^\infty \left(\frac{n(E,E_i)}{N_{in}} \right) E^2 dE} = \frac{M_1^2}{M_2} \tag{2.38}$$

where

$$M_j(E_i) = \int_0^\infty AED(E, E_i)E^j dE \tag{2.39}$$

is the j^{th} moment of the monoenergetic absorbed energy distribution $AED(E, E_i)$, defined as $n(E, E_i)$ normalized to the number of incident photons N_{in}.[15]

When a spectrum of photons is incident on the detector, Eq. (2.38) becomes

$$DQE = \frac{m_1^2}{m_2} \tag{2.40}$$

where

$$m_j = \int_0^\infty AED_s(E)E^j dE \tag{2.41}$$

is the j^{th} moment of the spectral absorbed energy distribution $AED_s(E)$, which could be found mathematically by averaging the monoenergetic distributions $AED(E, E_i)$ over the spectrum.

The DQE which has been described is known as the *zero-frequency* DQE, or $DQE(0)$. A more general quantity is $DQE(f)$, i.e. as a function of spatial frequency. In the case of the a-Se detector, as with phosphor-based systems, the detector is assumed to be sufficiently uniform and large such that absorption noise is not dependent on spatial frequency (white noise). This assumption could not be made for film, for example, because of the non-uniformity caused by the grains. Using this assumption and the fact that the signal is degraded by the MTF, leads to

$$DQE(f) = DQE(0) \cdot MTF^2(f) \,. \tag{2.42}$$

2.4.3 Scatter Fraction and Scatter-to-Primary Ratio

In portal imaging, the visibility of an anatomical object is of prime importance so that the treatment field can be compared with anatomical landmarks. To model this situation, consider an object of attenuation coefficient μ which is embedded in a water-equivalent phantom.[16] The difference in detector signal produced by in an area underneath the object

and from an adjacent region, ΔQ, is related to the visibility of the object in the final image. The contrast C in the final image compares this difference to the signal itself, i.e.

$$C = \frac{\Delta Q}{Q}, \tag{2.43}$$

and the differential signal-to-noise ratio $DSNR$ compares it to the noise σ in the image, i.e.

$$DSNR = \frac{\Delta Q}{\sigma}. \tag{2.44}$$

The signal is comprised of a portion due to the primary beam, Q_p, and a portion due to the scattered beam, Q_s, i.e.

$$Q = Q_p + Q_s \quad . \tag{2.45}$$

Assuming the presence of the object only changes Q_p, but does not alter Q_s negligeably, then $\Delta Q \approx \Delta Q_p$ and does not depend on the presence of scatter. By Equation (2.43), the decrease in contrast due to scatter is therefore

$$\frac{C_s}{C_{ns}} = \frac{Q_p}{Q_p + Q_s} = 1 - SF \tag{2.46}$$

where C_s and C_{ns} are the contrast with and without scatter, respectively, and the scatter fraction SF is defined as

$$SF = \frac{Q_s}{Q_s + Q_p}. \tag{2.47}$$

Using the same assumption, a similar factor can be found for the reduction in $DSNR$. In the presence of scatter, the standard deviation in the signal σ_Q will be given by

$$\sigma_Q = \sqrt{\sigma_{Q_p}^2 + \sigma_{Q_s}^2} \tag{2.48}$$

since scatter and primary signals are mutually exclusive. In the absence of scatter, Equation (2.48) simply becomes $\sigma_Q = \sigma_{Q_p}$. By Equation (2.44), this leads to

$$\frac{DSNR_s}{DSNR_{ns}} = \frac{1}{\sqrt{1 + SPR}} \tag{2.49}$$

where $DSNR_s$ and $DSNR_{ns}$ are the $DSNR$ with and withouth the presence of scatter, and the scatter-to-primary ratio SPR is defined as

$$SPR = \frac{\sigma_s^2}{\sigma_p^2} \quad . \tag{2.50}$$

These factors, SF and SPR, therefore describe how scattered radiation affects a specific detector's image quality, namely the contrast and differential signal-to-noise ratio. For a digital display system, the loss in contrast can often be compensated by contrast-enhancing algorithms. The loss in $DSNR$, however, must be compensated by an increase in dose. The increase in dose at a depth of d_{max} in the patient is given approximately by

$$\frac{D_s}{D_{ns}} = 1 + SPR\,, \tag{2.51}$$

where D_s and D_{ns} are the dose with and without the presence of scatter, respectively.

References

[1] H. E. Johns and J. R. Cunningham. *The Physics of Radiology*. Charles C. Thomas Publisher, 4th edition edition, 1983.

[2] J. W. Boag. Xeroradiography (review). *Phys. Med. Biol.*, 18:3–37, 1973.

[3] C. A. Klein. *J. Appl. Phys.*, 39:2029, 1968.

[4] R. C. Alig and S. Bloom. *J. Appl. Phys.*, 49:3476, 1978.

[5] W. Que and J. A. Rowlands. X-ray photogeneration in amorphous selenium: Geminate versus columnar recombination. *Phys. Rev. B*, 51:500–507, 1995.

[6] J. A. Rowlands, G. DeCrescenzo, and N. Araj. X-ray imaging using amorphous selenium: determination of x-ray sensitivity by pulse height spectroscopy. *Med. Phys.*, 19:1065–1069, 1992.

[7] D. Mah. *Portal Imaging with Amorphous Selenium: A signal and noise analysis and comparison with fluoroscopic systems*. PhD thesis, University of Toronto, 1997.

[8] T. Falco, H. Wang, and B. G. Fallone. Preliminary study of a metal/a-Se –based portal detector. *(submitted to Med. Phys.)*, 1997.

[9] W. R. Nelson, H. Hirayama, and D. W. O. Rogers. The EGS4 code system. *Stanford Linear Accelerator Center Report, SLAC 265*, 1985.

[10] D. W. O. Rogers and A. F. Biejalew. *The Dosimetry of Ionizing Radiation*. edited by K. R. Kase, B. E. Bjarngard, and F. H. Attix, Academic, New York, 1989.

[11] A. F. Biejalew and D. W. O. Rogers. PRESTA — the parameter reduced electron-step algorithm for electron Monte Carlo transport. *Nucl. Instrum. Methods B*, 18:165–181, 1989.

[12] R. N. Bracewell. *The Fourier Transform and its Applications*. McGraw-Hill Book Company, 2nd edition edition, 1978.

[13] J. C. Dainty and R. Shaw. *Image Science*. Academic Press, London, New York, 1974.

[14] R. T. Droege and B. E. Bjängard. Metal screen-film detector MTF at megavoltage x-ray energies. *Med. Phys.*, 6(6):515–518, 1979.

[15] R. Swank. Absorption and noise in x-ray phosphors. *J. Appl. Phys*, 44:4199–4203, 1973.

[16] W. Swindell, E. J. Morton, P. M. Evans, and D. G. Lewis. The design of megavoltage projection imaging systems: Some theoretical aspects. *Med. Phys.*, 18:855–866, 1991.

Chapter 3: Procedure

3.1 Primary Beam

3.1.1 Exit Spectrum

To properly model the response of the detector to the primary beam, the energy spectrum of the primary photons transmitted through the patient is required. The hardening of the spectrum from the linear accelerator head, referred as the entrance spectrum, was approximated by assuming the patient to be equivalent to 20 cm polystyrene.

The entrance spectrum used was a 6 MV Monte Carlo generated distribution taken from Kubsad *et al*,[1] shown in Fig. 14. A simple EGS4 user code was written to calculate the primary exit spectrum with the geometry (coded in HOWFAR) shown in Fig. 2. The MAIN program and AUSGAB are shown in Figs 3 and 4, respectively. A pencil beam of photons with energies sampled from the entrance spectrum was incident perpendicularly

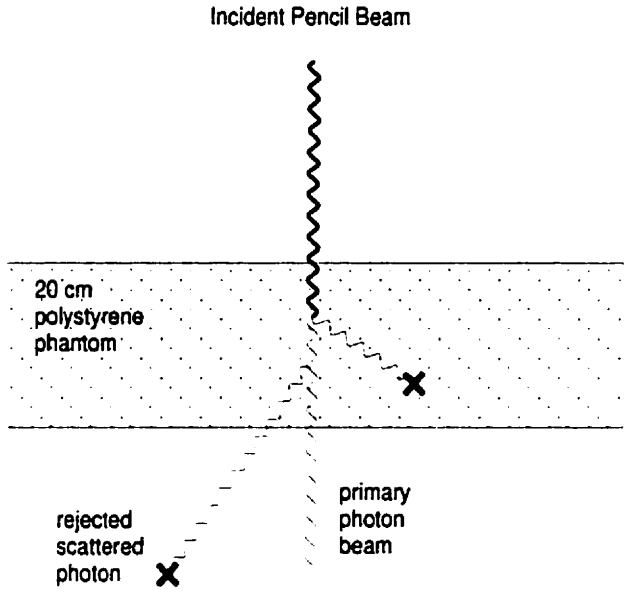

Figure 2: EGS4 user code geometry simulate the exit spectrum of a 6 MV beam through a 20 cm polystyrene phantom

to a 20 cm polystyrene slab. Only primary photons which came out on the exit side of the slab were scored. This was accomplished by determining which photons were about to undergo either Rayleigh scattering, photoelectric scattering, Compton scattering or pair production by verifying which IARG value was passed to AUSGAB, and labelling those particles with a LATCH variable (which would subsequently be passed on to its progeny). Only photons with LATCH=0 were then scored, which corresponded to the primary beam. These photons were sorted according to their energy in 25 keV bins to form the primary exit spectrum.

The simulations in this and all other user codes in this work were run with energy cutoffs corresponding to 10 keV of total energy, i.e. photon cutoffs of PCUT = 10 keV

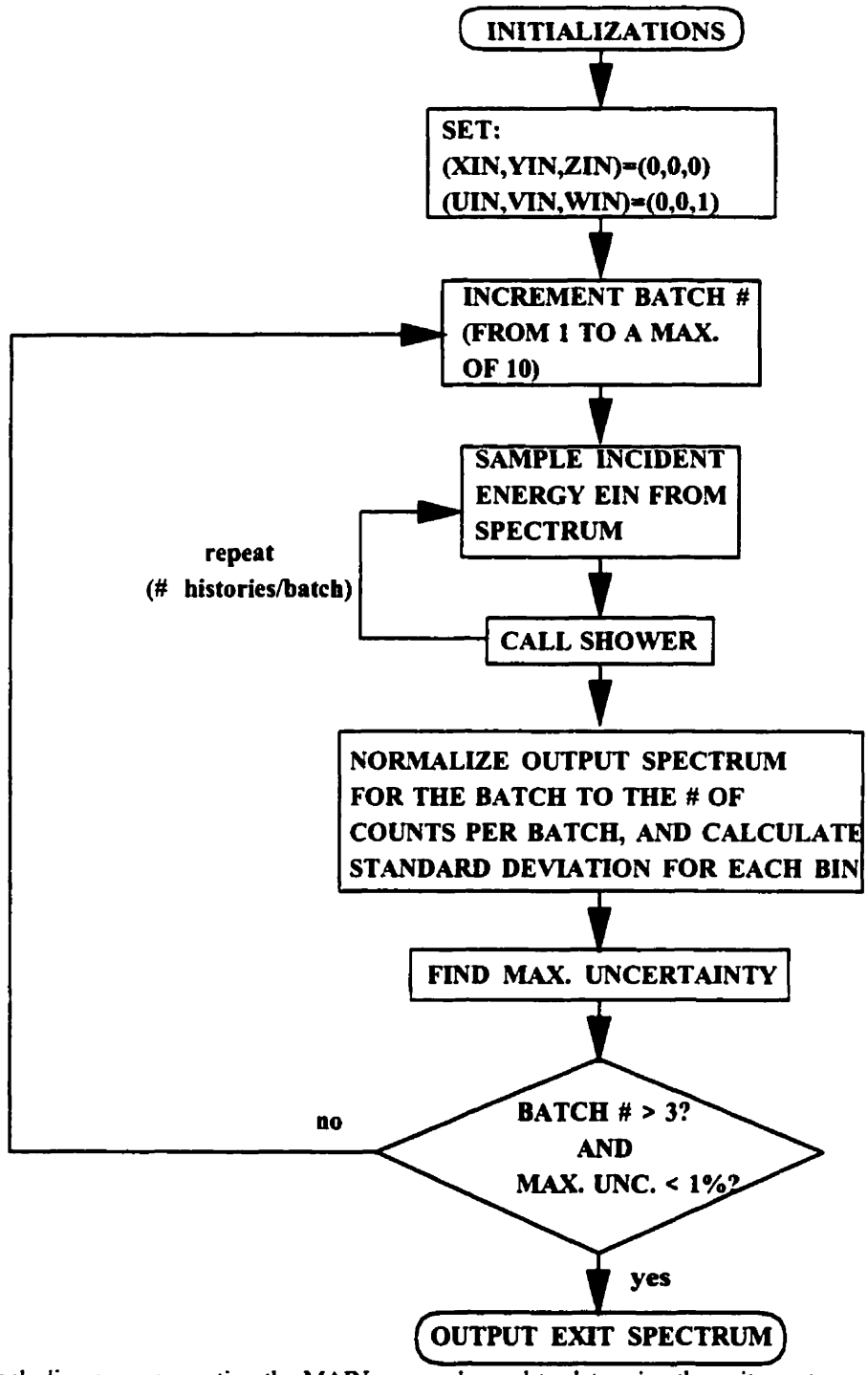

Figure 3: Block diagram representing the MAIN user code used to determine the exit spectrum

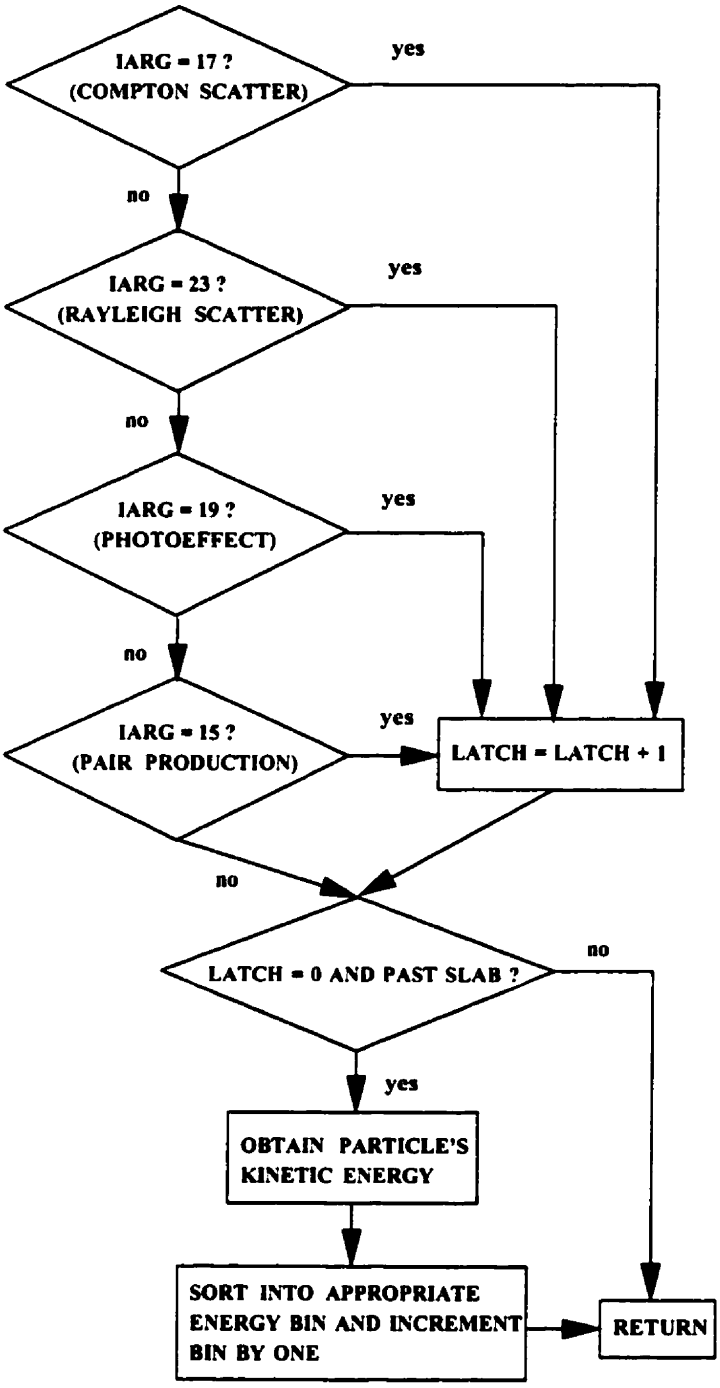

Figure 4: Block diagram representing the AUSGAB subroutine used to determine the exit spectrum

and electron cutoffs of ECUT = 521 keV. These values proved to be a good balance between accuracy and computer time. Rayleigh scattering was neglected since it did not significantly affect the results, except in the exit spectrum simulations (since it was only run a limited number of times and therefore time was not a major factor). PRESTA was used to make the simulations less dependent on step-size and to decrease simulation time. We used improved sampling of the Bremsstrahlung angular distribution,[2] and improved ICRU stopping power values[3, 4] which included density-effect corrections. The number of histories were divided into 10 batches, with sufficient histories to achieve standard deviations of less than 1% in each bin.

3.1.2 Zero-Frequency Detective Quantum Efficiency Simulations

The detector was modelled as a semi-infinite metal plate of variable thickness over a 0.3 mm surface of atomic Selenium with a reduced density of 4.27 g/cm^3. The metal plates used in the simulations were Copper, Tungsten, Lead and Aluminum.

Since the energy deposition in the metal/a-Se detector is analogous to that in a metal/phosphor detector (assuming an average $\overline{W}$, i.e. no energy dependence — See Section 2.2), the $DQE(0)$ was simulated in a manner similar to Jaffray *et al*,[5] by replacing the phosphor layer with Selenium. An EGS4 user code with geometry shown in Fig. 5 was written for this purpose; MAIN and AUSGAB are shown in Figs 6 and 7, respectively. An input pencil beam with energy sampled from the exit spectrum was

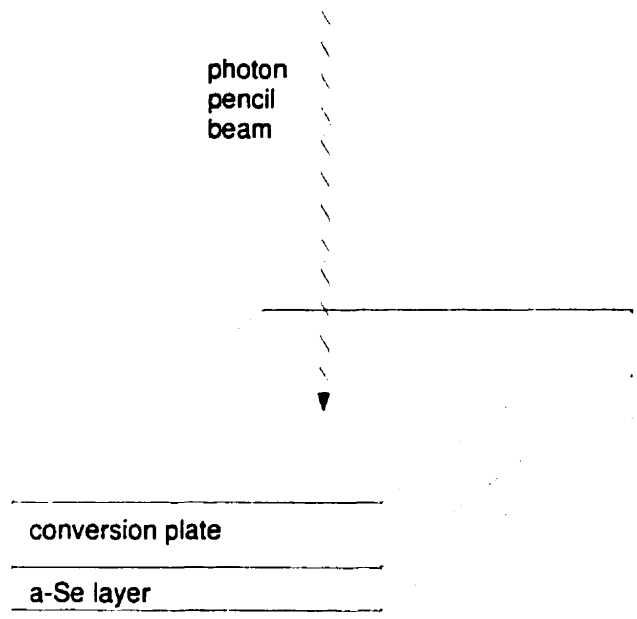

Figure 5: EGS4 user code geometry to simulate $DQE(0)$

incident perpendicularly to the detector. A variable in EGS4 called EDEP provides the energy deposited in a particular call to AUSGAB; the total energy deposited in the Selenium layer per history was determined by summing up each of these contributions in the shower in a variable called EABS. This quantity was then binned with a bin width of 10 keV. This distribution, normalized to the incident number of photons, represents the spectral absorbed energy distribution $AED_s(E)$.

The $DQE(0)$ was calculated from the output of the user code with Eq. (2.40) for the following cases:

i) To compare between using an entrance or exit spectrum, simulations were run for both cases with a 1 mm Cu / 0.3 mm a-Se detector

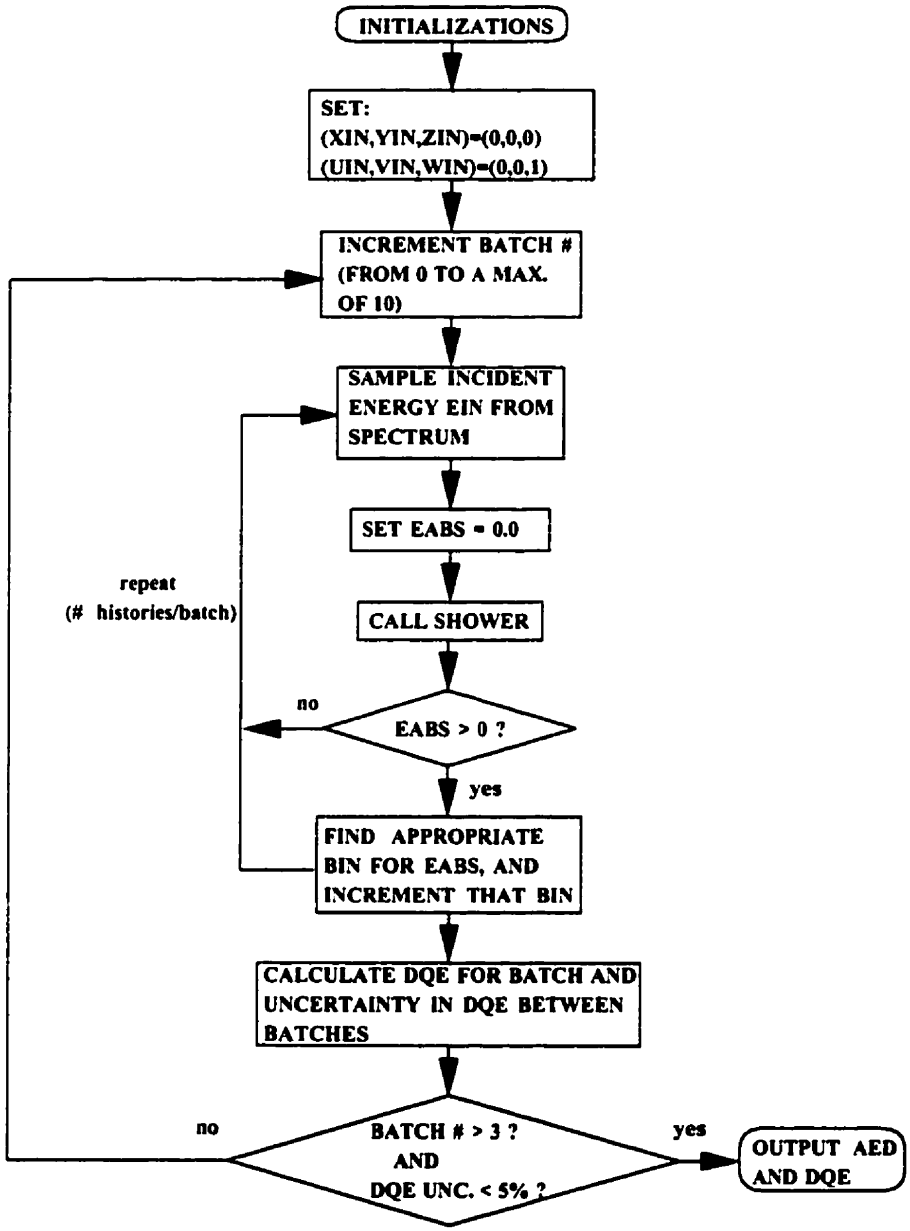

Figure 6: Block diagram representing the MAIN program used to determine the AED and DQE

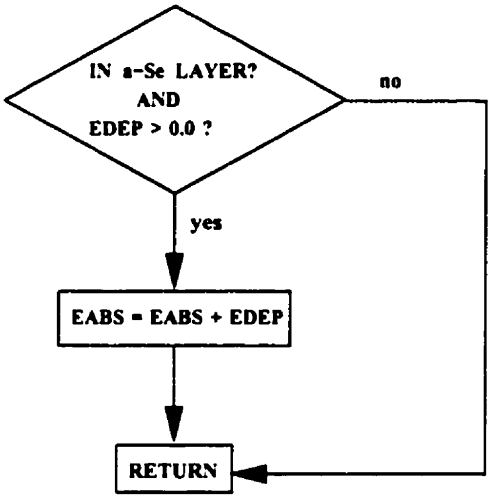

Figure 7: Block diagram representing the AUSGAB subroutine used to determine the AED and DQE

ii) The four metal plate types (Cu, W, Pb, Al) with varying build-up thickness (0.3 mm a-Se)

iii) Varying a-Se thickness with a fixed Cu front plate thickness (repeated for 0.5, 1.0 and 1.7 mm Cu)

iv) To compare directly with the work of Munro *et al*[6], the simulation was performed with the entrance 6 MV spectrum, a 1 mm front Cu plate and the Selenium layer was replaced with 400 mg/cm^2 Gadolinium Oxysulfide (Gd_2O_2S with a density of

3.67 g/cm^2)

v) Comparison with the entrance spectrum between 1 mm Cu with 400 mg/cm^2 (0.937 mm) Gd_2O_2S and 0.3 mm a-Se. Also, a simulation was run with 0.8 mm Cesium Iodide (CsI), another phosphor (ρ = 4.5 g/cm^3)

Sufficient histories were run to produce an uncertainty less than 5% in $DQE(0)$. Simulation time ran from 4 to 48 hours on an SGI workstation (IRIS INDIGO, Silicon-Graphics, Mountainview, CA).

3.1.3 Modulation Transfer Function Simulations and Determination of $DQE(f)$

To simulate the $MTF(f)$, an EGS4 user code with HOWFAR geometry shown in Fig. 8, and MAIN and AUSGAB block diagrams shown in Figs 9 and 10, was written. A photon line source with a width of 2 μm is incident perpendicular to the detector and the photon energies are sampled from the exit spectrum. The source width was chosen to ensure that the $sinc$ function degradation due to the finite width in Eq. (2.30) does not alter the MTF below 10 cycles/mm by more than 2%. The Selenium was separated into 5 μm strips for up to a distance of 1 mm on either side. A rule of thumb to ensure that Molière Theory, which is used in EGS4 to determine the new direction for an electron at the end of a transport step, is valid is to ensure that the number of multiple scattering

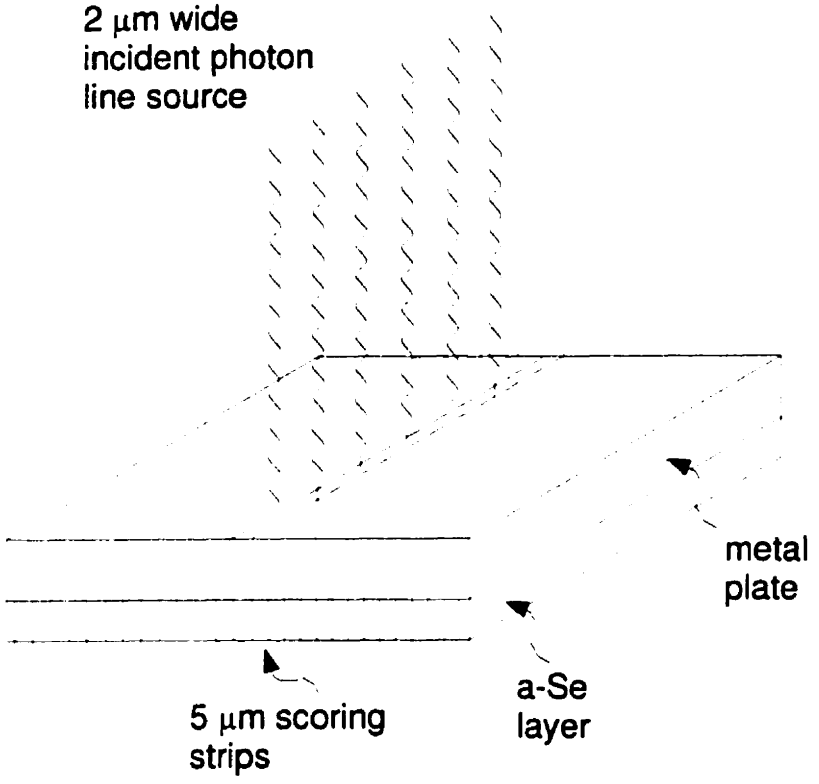

Figure 8: EGS4 user code geometry to simulate $MTF(f)$

events N_{ms}, which is approximately given by

$$N_{ms} = density(g/cm^3) \cdot (Z/8)^{\frac{1}{3}} \cdot stepsize(\mu m) \quad , \tag{3.1}$$

is at least 20. For a-Se, for a 5 μm step-size, this works out to be approximately 35, which is sufficient.

The dose in each strip was scored to within 5%: the uncertainty being calculated by splitting the histories into 10 batches and determining the standard deviation. The dose in adjacent strips were averaged to satisty the condition of Eq. (2.33). Symmetry on either side of the line source was assumed, and any energy deposited on one side was

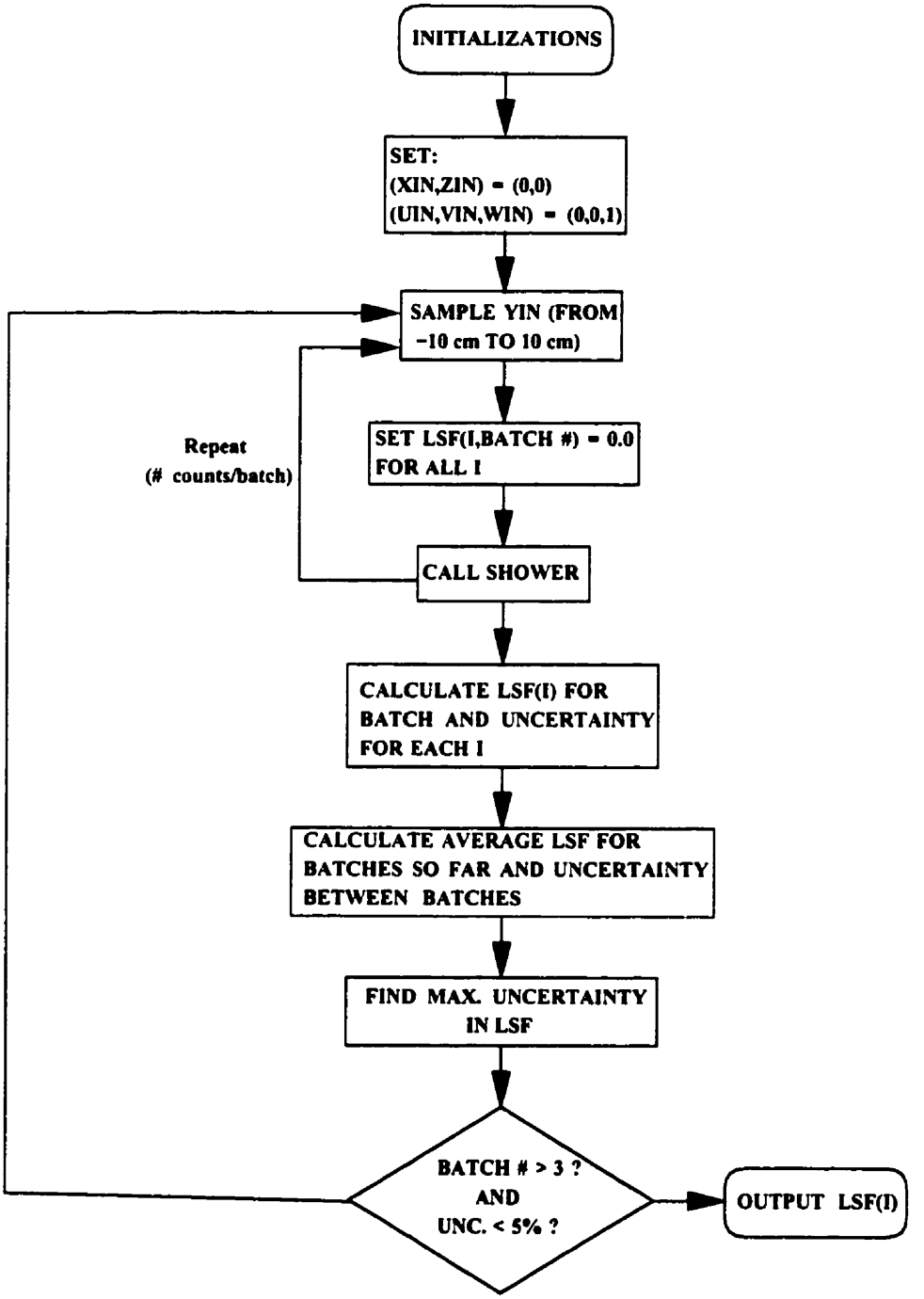

Figure 9: Block diagram representing the MAIN program used to determine the LSF (and MTF)

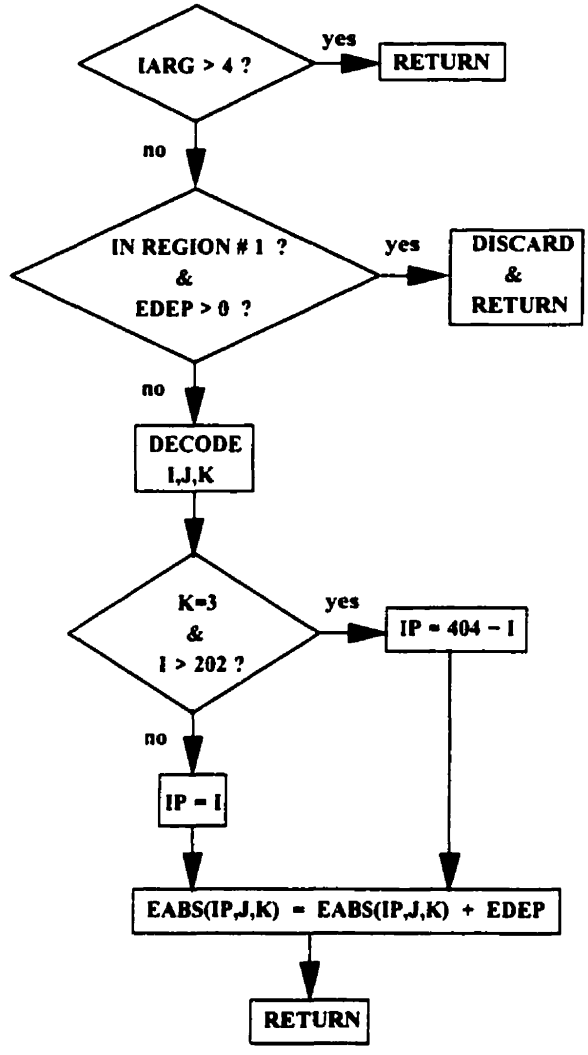

Figure 10: Block diagram representing the AUSGAB subroutine used to determine the LSF (and MTF)

deposited on the corresponding strip on the other side to reduce simulation times. The sides were then taken as mirror images of each another.

The resulting dose distribution was normalized to unit area and represents the discrete $LSF(x)$ due to energy absorption. The $MTF(f)$ was found by performing a Fast Fourier Transform (FFT) of the $LSF(x)$. Simulations were run for the same cases as for $DQE(0)$, and $DQE(f)$ was subsequently calculated with Eq. (2.42).

3.2 Patient Scatter

3.2.1 Scatter Fraction and Scatter-to-Primary Ratio Simulations

The quantities SF and SPR were modelled with the geometry shown in Fig. 11. Block diagrams for MAIN and AUSGAB are shown in Figs 12 and 13. The photons originate from a point source with a direction sampled such that all photons are incident with even probability onto a square 20 × 20 cm^2 field defined at a source-to-surface distance (SSD) of 100 cm. The photon energy is sampled from the same 6 MV spectrum used to determine the exit spectrum. The change of spectrum with angle and the beam profile are not considered since energy deposition will only be calculated close to the central axis where these effects are not important.

A 20 cm slab of polystyrene is defined at SSD = 100 cm, and the detector is modelled in the same way as for the $MTF(f)$ and $DQE(0)$ simulations, with a source-to-receptor

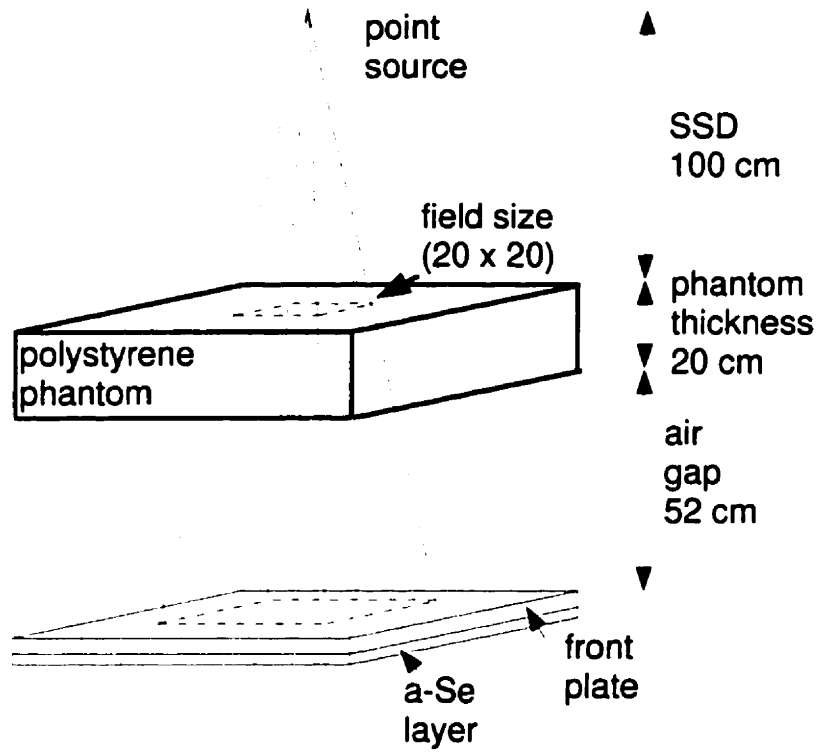

Figure 11: EGS4 user code geometry to simulate the SF and SPR

distance (SRD) of 172 cm. The sensitive region of interest (ROI) in which dose is scored is defined as the central 5 × 5 cm^2 of the detector.

Primary photons and scattered particles originating from the polystyrene slab are labelled separately with the use of the LATCH variable, in the same way as for the exit spectrum simulations except that the scattered particles are not removed off the stack. For each history, the energy deposited in the central ROI of the detector by primary photons is scored with a variable E_{i_p} (or EABS(1) in the actual code), and the energy deposited by the scattered beam is scored with a variable E_{i_s} (EABS(2) in the code). When N histories have been completed, the average and standard deviation (using Poisson statistics) in the

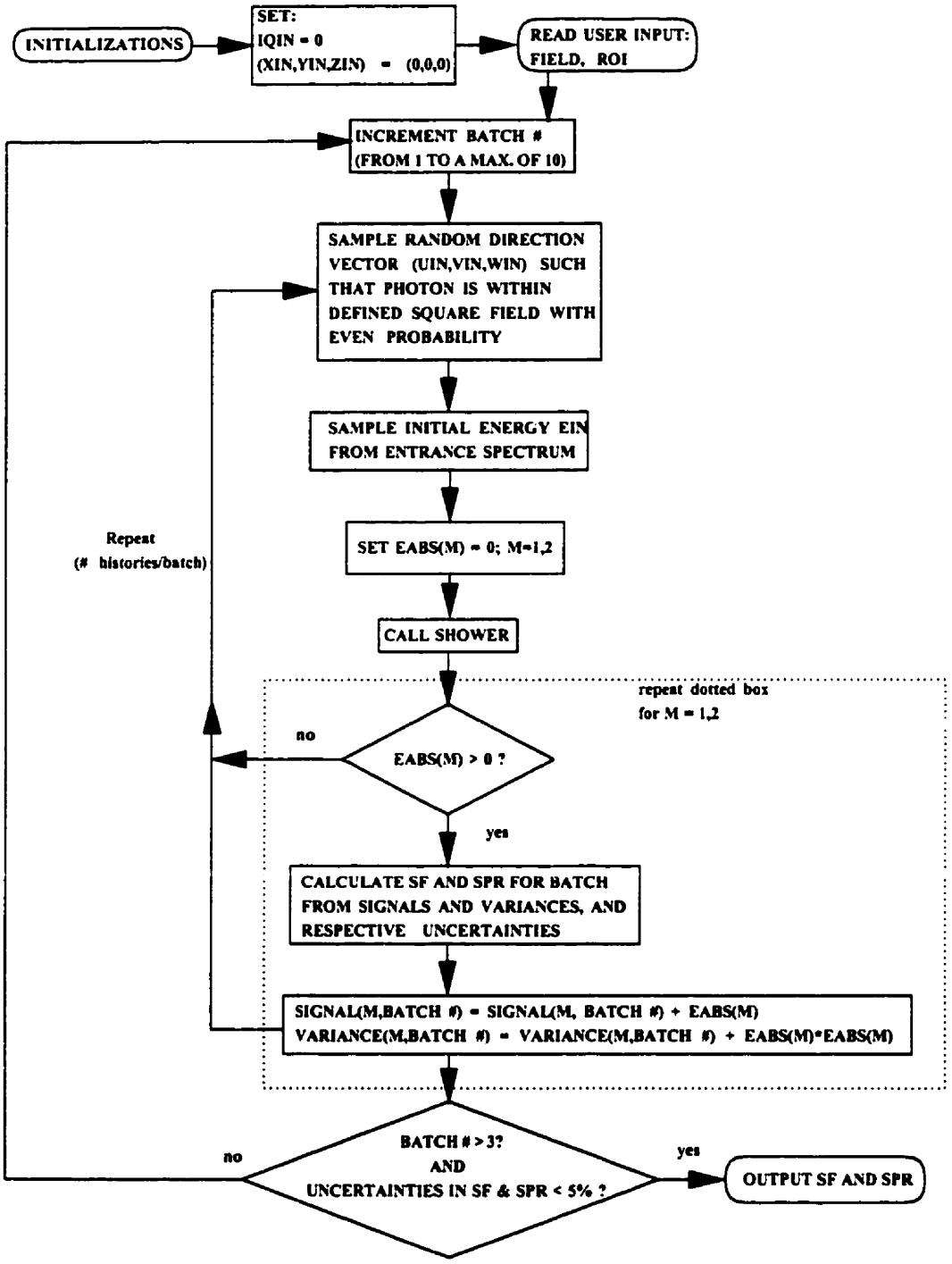

Figure 12: Block diagram representing the MAIN user code used to determine the SF and SPR

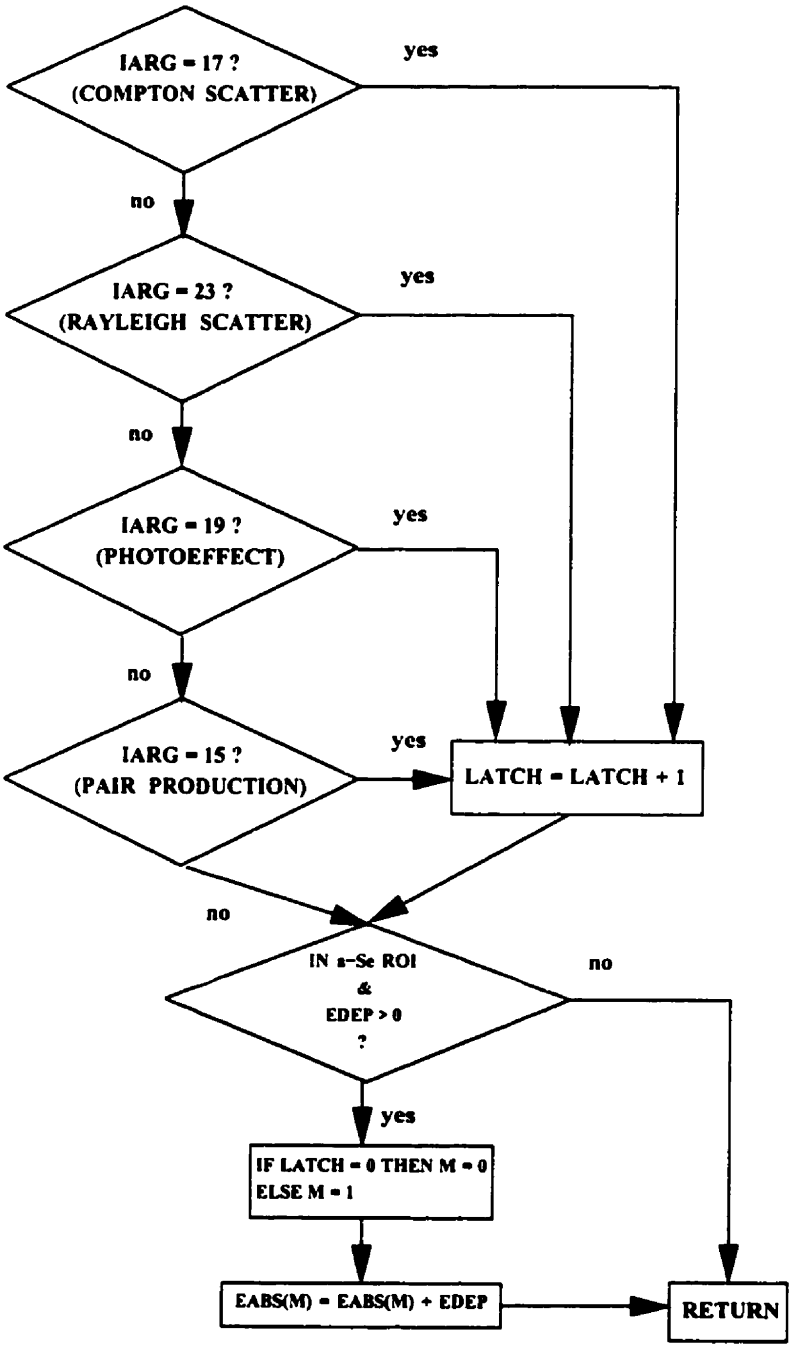

Figure 13: Block diagram representing the AUSGAB subroutine used to determine the SF and SPR

energy deposited due to the primary and scattered beams are calculated as

$$E_{p,s} = \frac{1}{N}\sum_{i=1}^{N} E_{i_{p,s}} \tag{3.2}$$

and

$$\sigma_{E_{p,s}} = \sqrt{\frac{1}{N}\sum_{i=1}^{N} E_{i_{p,s}}^2} \quad . \tag{3.3}$$

The EGS4 parameters and configurations used are the same as for the MTF and DQE user codes, discussed in Section (II-A-2). Simulations required between 8 and 48 hours.

3.2.2 Measurement of Scatter Fraction

Description of Imager

The imager consists of a light-tight box with a 20 × 20 cm^2 which holds the metal/a-Se plates. Scanning is performed by a servo-motor operated two-dimensional motion stage, which is controlled by a two axis microprocessor-based motion controller (Unidex11, Aerotech, Inc., Pittsurgh, PA) capable of 2 μm positional accuracy. An electrostatic coupling probe (Trek Inc., model P0766/344, Medina, NY), with an aperture width of 200 μm and the capability to measure potentials up to 3000 V, is installed on this stage and is positioned at a distance of approximately 100 μm from the a-Se surface. The probe output is digitized via a 16–bit analog-to-digital converter (ADC488/16A, Iotech). The stage motion and data acquistion are controlled by a commercial package (LABVIEW, National Instruments, Inc., Austin, TX) on a 486 Personal Computer.

Also installed on the motion detector is a scorotron, which consists of three fine conducting wires set to a high potential (6550 V) above a wire mesh grid set to 2100 V. The wires cause electrical breakdown of the surrounding air, resulting in charge carriers. Negatively charged carriers (mostly CO_3^-) subsequently drift in the electric field created by the grid towards the a-Se surface, where they become trapped. To charge the plate, the motion controller sweeps the scorotron (which is 2 mm above the a-Se surface) three times across the plate, resulting in an even accumulation of charge on the a-Se surface. After this procedure, a surface potential equal to the grid potential (2100 V) is achieved.

After irradiation, the remaining surface voltage distribution is performed by scanning the probe over a 13" × 13" in a raster fashion, with a measurement sample of 200 × 200 points (approximately 650 μm intervals).

Measurement Procedure

The measurement of the voltage at the surface of the a-Se layer represents the signal. A calibration curve was obtained to linearize this signal into relative absorbed dose.

The imager was placed under the 6 MV beam of a Clinac 2300 C/D linear accelerator, such that the distance between the source and the top of the plate was 172 cm. For each measurement point, the plate was charged to an initial voltage V_o of 2100 V via corona charging. The imager was then exposed with a 10 × 10 cm^2 field (defined at 100 cm from

the target) to an increasing number of monitor units (MU*), and the resulting average plate voltage in a 5 × 5 cm^2 ROI at the centre of the plate was measured with the scanning electrostatic coupling probe. Since the dose deposited in the a-Se is directly proportional to the number of monitor units, plots of plate voltage versus relative dose to the a-Se were obtained. The calibration was performed for the following front plates:

i) 1.0 mm Copper

ii) 1.5 mm Copper

iii) 2.0 mm Aluminum

iv) 1.0 mm Tungsten,

each with a 0.3 mm a-Se layer.

To measure the Scatter Fraction, a polystyrene phantom was placed at SSD = 100 cm perpendicular to the 6 MV Clinac 2300 C/D beam. The detector was placed at SRD = 172 cm. The plate voltage remaining in the central ROI after a fixed MU irradiation (approximately 7 MU, depending on the plate), $V'(A)$, was measured with the probe for field sizes A varying from 2 × 2 cm^2 to 20 × 20 cm^2, and converted to $D'(A)$ with the dose-response curve. The lower limit was determined by the size of the beam penumbra which interfered with the ROI, and the upper limit by the size of the phantom.

---

* A linear acclerator's output is measured in Monitor Units (MU), calibrated such that one Monitor Unit (MU) results in 1 cGy for a 10 × 10 cm^2 field in tissue at SSD = 100 cm.

This was repeated three times for each of the four plates; the standard deviation of the trials was used to estimate the uncertainty.

The curve $D'(A)$ was then extrapolated to zero-area field by the use of a weighted second-order polynomial to find the contribution of the primary beam, $D'(0)$. The uncertainty in this quantity, $\delta D'(0)$, was taken as the y-axis uncertainty calculated by the fitting program. The curve was then normalized to $D'(0)$ so that the relative dose at zero-field was unity.

In calculating the scatter fraction, it is only the effects of patient scatter that must be considered. However, $D'(A)$ is expected to increase not only due to an increase in patient scatter with field size but also to an increase in the linear accelerator output factor. To correct for this, the same experiment was repeated with the absence of the phantom. The resulting curve $D_c(A)$, also normalized to unity at zero field, represents the increase in a-Se dose with field size which is not due to patient scatter. Consequently, the dose variation with field size due only to the effects of patient scatter, $D(A)$, is approximately given by

$$D(A) = \frac{D'(A)}{D_c(A)} \quad . \tag{3.4}$$

The uncertainty $\delta D(A)$ is given by

$$\delta D(A) = D(A) \cdot \sqrt{\left(\frac{\delta D'(A)}{D'(A)}\right)^2 + \left(\frac{\delta D_c(A)}{D_c(A)}\right)^2} \quad . \tag{3.5}$$

From the corrected curve, the scatter fraction for a 20 × 20 cm^2 can then be calculated. Since $D(20)$ represents the total dose, and $D(0)$ the primary dose, then the difference represents the scatter dose. From Eq. (2.47), the scatter fraction is then given by

$$SF(20) = \frac{D(20) - D(0)}{D(20)} \quad . \tag{3.6}$$

The uncertainty was then calculated by

$$\delta SF = \frac{D(20)}{D(0)} \cdot \sqrt{\left(\frac{\delta D(20)}{D(20)}\right)^2 + \left(\frac{\delta D(0)}{D(0)}\right)^2} \quad . \tag{3.7}$$

The scatter fraction was measured in this fashion for each of the four plates. One factor in this measurement which is arbitrary is the amount of MUs used. Assuming the dose-response curve accurately linearizes the signal, this factor should make no difference. To check the validity of this technique, however, the experiment was repeated with different MUs to expose the plate, both with and without the presence of the phantom.

References

[1] S. Kubsad, R. Mackie, B. Gehring, D. Misisco, B. Paliwal, M. Mehta, and T. Kinsella. Monte carlo and convolution dosimetry for stereotactic radiosurgery. *Int. J. Radiat. Oncol. Biol. Phys*, 19:1027–1035, 1990.

[2] A. F. Biejalew, R. Mohan, and C-S. Chui. Improved bremsstrahlung photon angular sampling in the EGS4 code system. *National Research Council of Canada, Division of Physics Report*, PIRS-0203, 1989.

[3] D. W. O. Rogers, S. Duane, A. F. Bielajew, and W.R. Nelson. Use of ICRU-37/NBS radiative stopping powers on the EGS4 system. *National Research Council of Canada, Division of Physics Report, PIRS-0177*, 1989.

[4] S. Duane, A. F. Bielajew, and D. W. O. Rogers. Use of ICRU-37/NBS collisional stopping powers on the EGS4 report. *Use of ICRU-37/NBS Collisional Stopping Powers on the EGS4 Report, PIRS-1073*, 1989.

[5] D. A. Jaffray, J. J. Battista, A. Fenster, and P. Munro. X-ray scatter in megavoltage transmission radiography: Physical characteristics and influence on image quality. *Med. Phys.*, 21:45–60, 1994.

[6] P. Munro, J. A. Rawlinson, and A. Fenster. Therapy imaging: A signal-to-noise analysis of fluoroscopic imaging system for radiotherapy localization. *Med. Phys.*, 17:763–772, 1990.

Chapter 4: Results and Discussion

4.1 Exit Spectrum

The 6 MV entrance spectrum taken from Kubsad *et al*[1] and the exit spectrum determined with EGS4 for a 20 cm polystyrene phantom are shown in Fig. 14. The average energy increases from 2.23 MeV to 2.73 MeV. The $DQE(f)$ resulting from the entrance and exit spectra are shown in Fig. 15. The $DQE(f)$ is seen to be degraded over all frequencies when the exit spectrum is used, mostly due to a lower MTF.

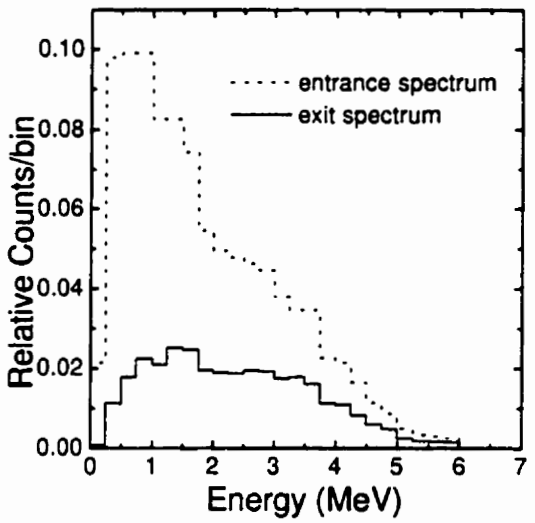

Figure 14: 6 MV entrance spectrum (Kubsad *et al*[21]) and primary exit spectrum through 20 cm polystyrene phantom generated with EGS4. Both spectra are normalized to the total number of incident photons

4.2 Absorbed Energy Distributions

Some sample $AED_s(E)$ distributions for different Cu and a-Se thicknesses are shown in Figs 16–19. In each distribution, there is a peak at an energy E_{peak} which depends on the a-Se thickness and not the copper thickness. This peak can be explained as follows: on average, the energy is transferred to an electron in the metal plate by the Compton effect, which is the most common interaction; this would not depend on metal thickness. This

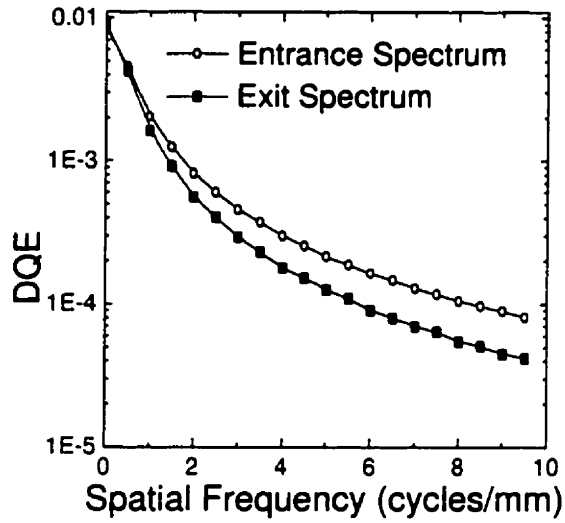

Figure 15: $DQE(f)$ for a 1 mm Cu / 0.3 mm a-Se detector for a 6 MV beam; comparison between using the DQE resulting from the entrance spectrum and that from the exit spectrum (20 cm polystyrene).

electron will subsequently deposit its energy in the a-Se, in an amount given roughly by

$$E_{peak} = \overline{S}\rho d \tag{4.1}$$

where $\overline{S}$ is the average collisional electron mass stopping power of a-Se, and ρ and d are the density and thickness of a-Se, respectively.

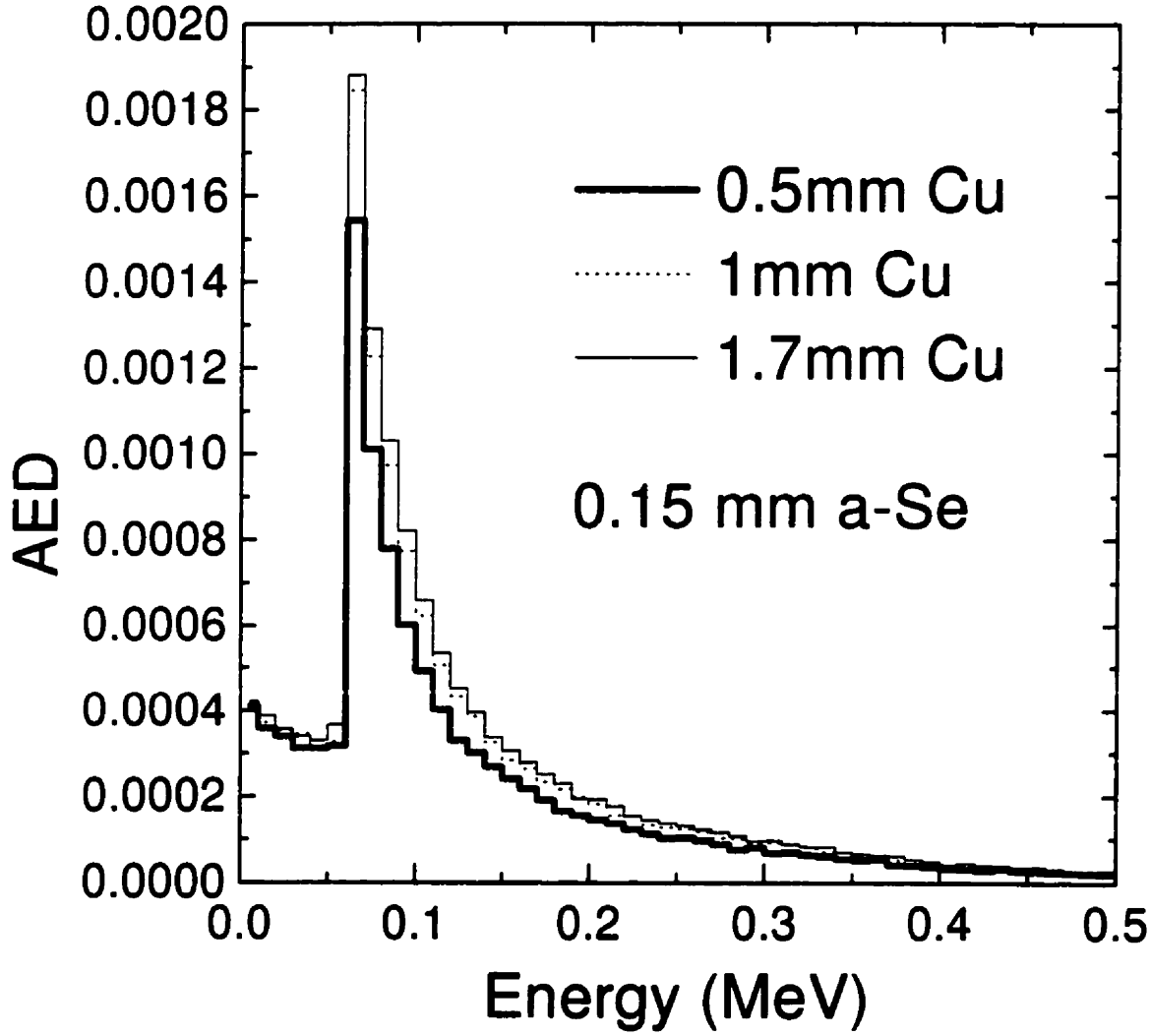

Figure 16: EGS4–generated Spectral Absorbed Energy Distribution $AED_s(E)$ for 0.15 mm a-Se, with three buildup thicknesses of copper

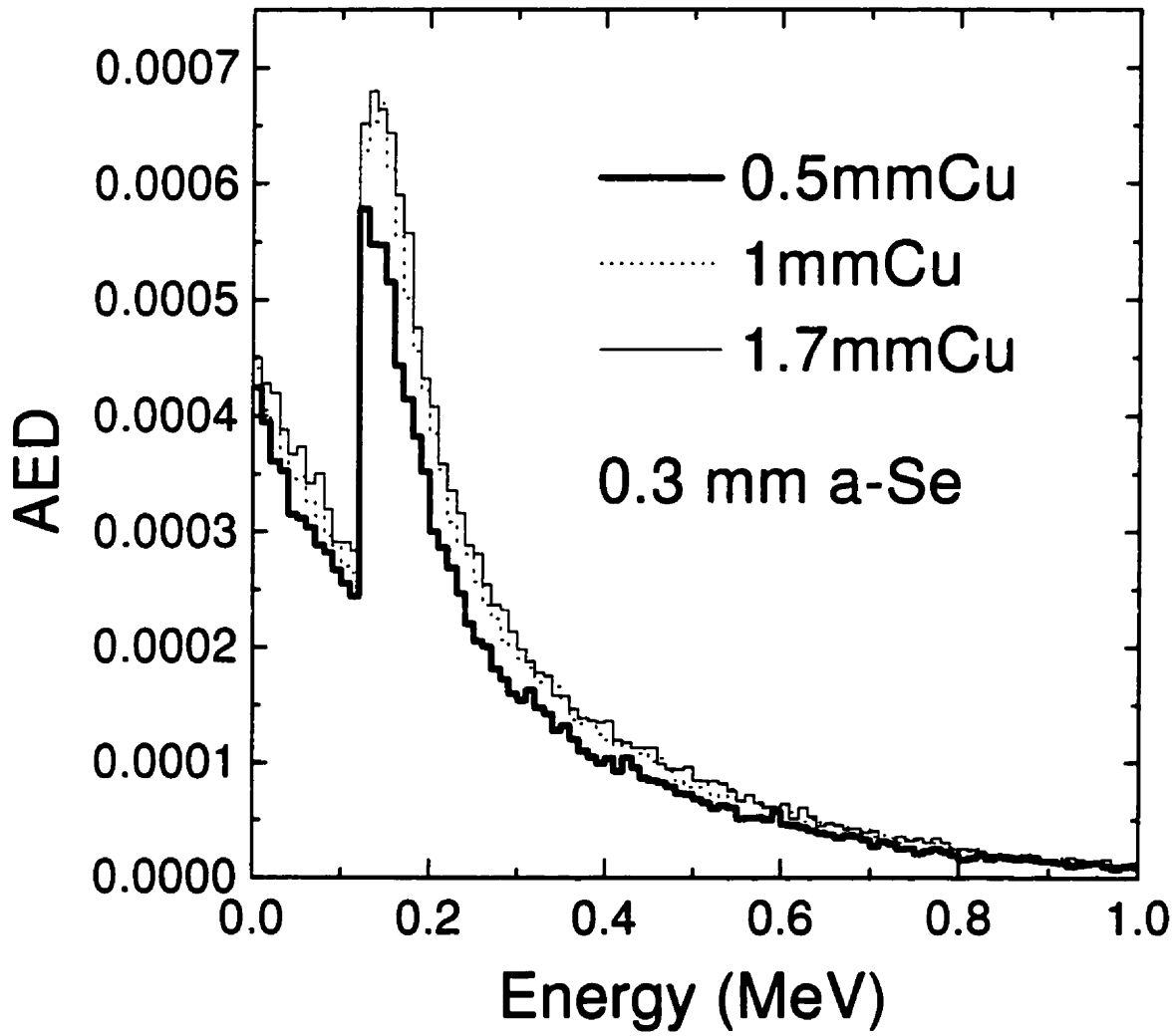

Figure 17: EGS4–generated Spectral Absorbed Energy Distribution $AED_s(E)$ for 0.3 mm a-Se, with three buildup thicknesses of copper

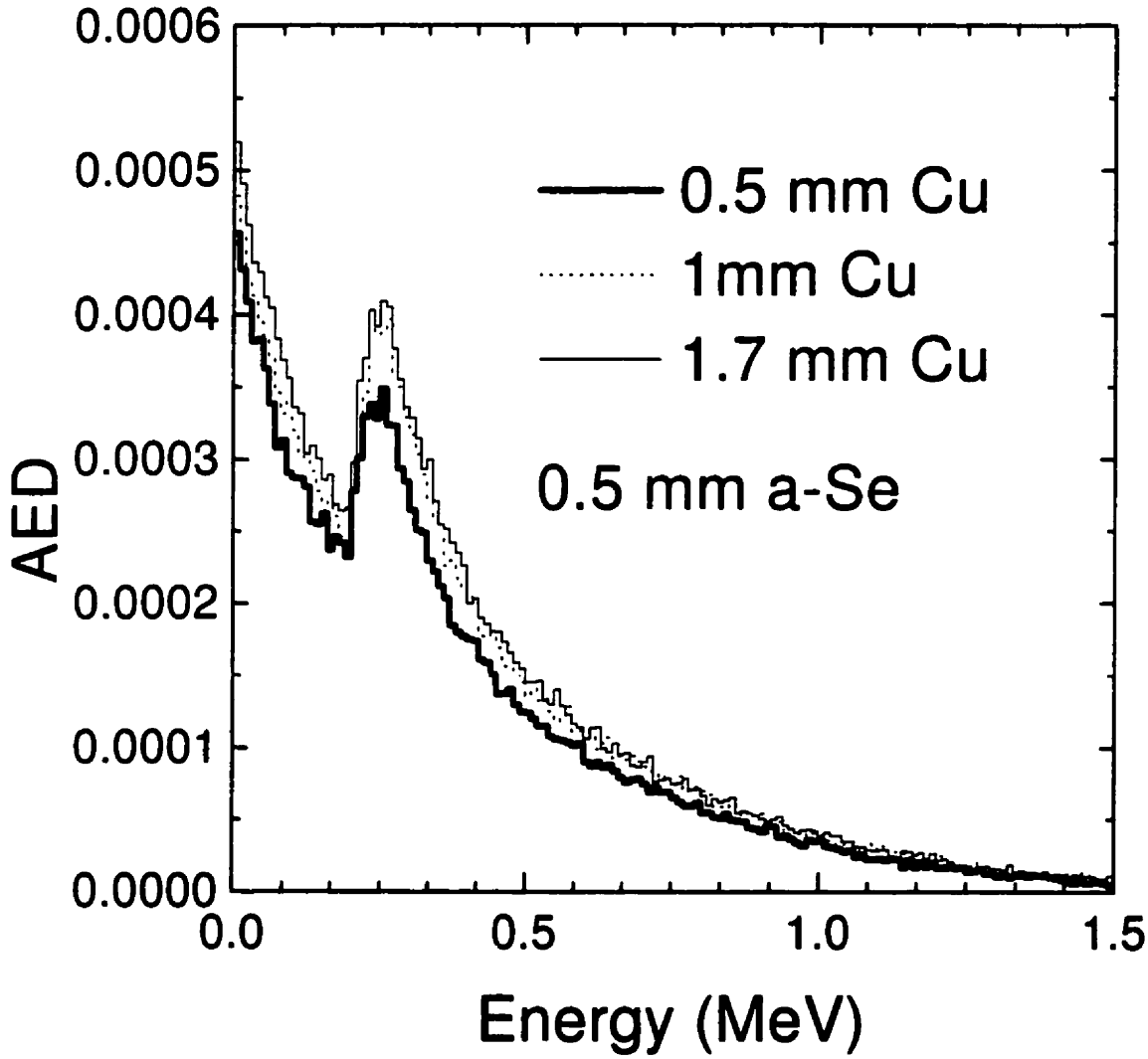

Figure 18: EGS4–generated Spectral Absorbed Energy Distribution $AED_s(E)$ for 0.5 mm a-Se, with three buildup thicknesses of copper

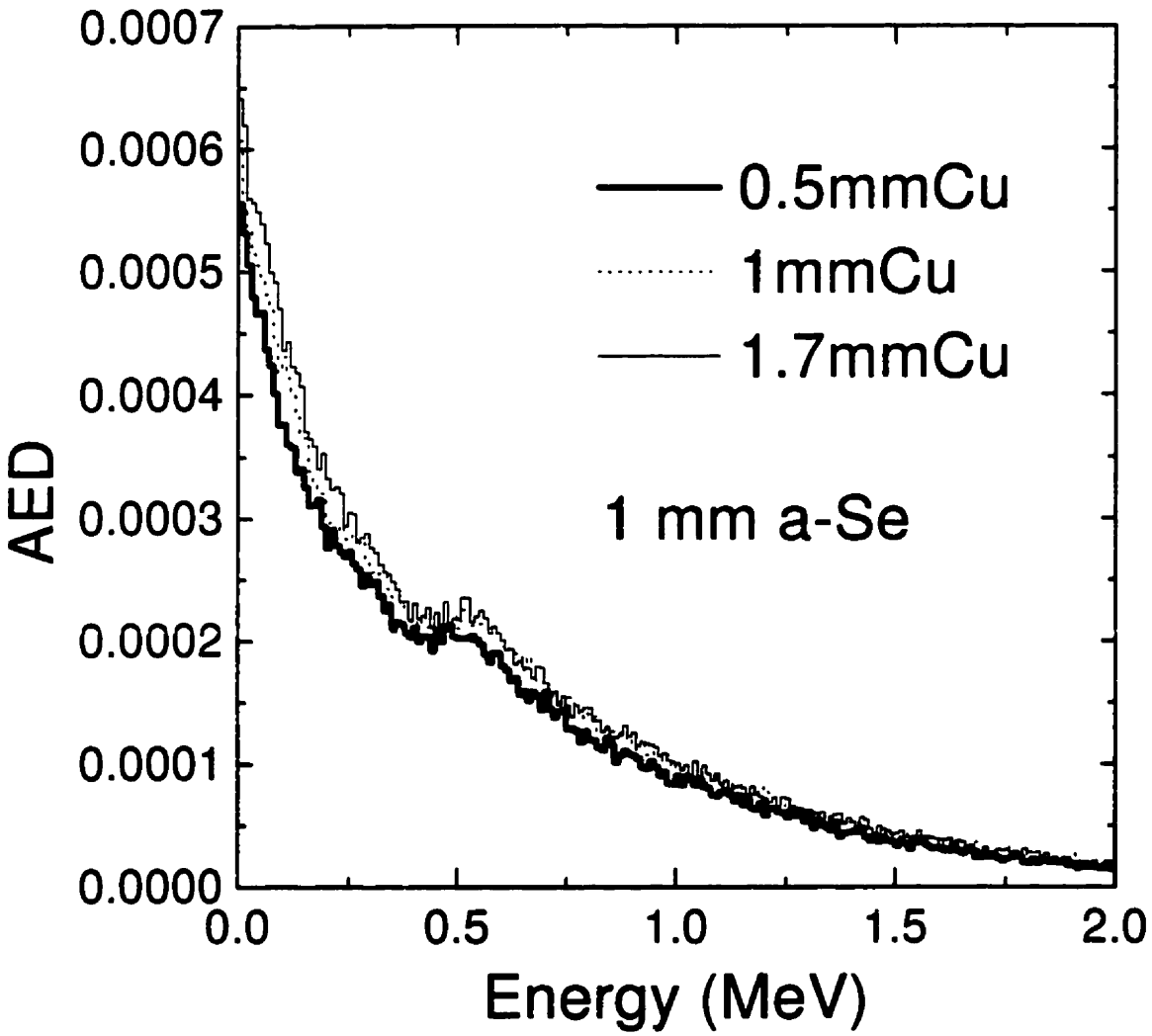

Figure 19: EGS4–generated Spectral Absorbed Energy Distribution $AED_s(E)$ for 1.0 mm a-Se, with three buildup thicknesses of copper

Using a stopping power $\overline{S}$ for a-Se of 1.3 Mev·cm^2/g†, Eq. (4.1) predicts a peak at approximately 0.55 MeV per millimetre. The peaks of Figs 16–19 occur at approximately this energy. As the a-Se thickness increases, the peak is seen to be more diffuse and less prominent when compared to the rest of the curve. This is expected since more interactions would take place in the a-Se causing a greater randomness of events. Increasing the metal thickness raises the magnitude of each bin, but does not change the overall general shape of the curve.

4.3 Detective Quantum Efficiency

The $DQE(f)$ simulated using the Kubsad *et al* entrance spectrum for the 1 mm Cu/ 400 mg/cm^2 phosphor combination is shown in Fig. 20(a), and is compared to the experimental results of the total $DQE(f)$ measured by Munro *et al.*[3] As expected, the EGS4 curve lies above the measured curve since it ignores processes such as light production and transport within the phosphor. The energy absorption curve forms an "upper limit" to the total DQE. Jaffray *et al*[4] have simulated $DQE(0)$ for the same situation, but did not consider spatial degradation. They obtained good agreement at zero frequency and stipulated that light production and transport do not affect the low-frequency DQE. Our simulations agree closely with the measured values up to about 1

† This value was found by scaling the stopping power of Copper[2], which has a similar atomic number to Selenium, and scaling by the appropriate density

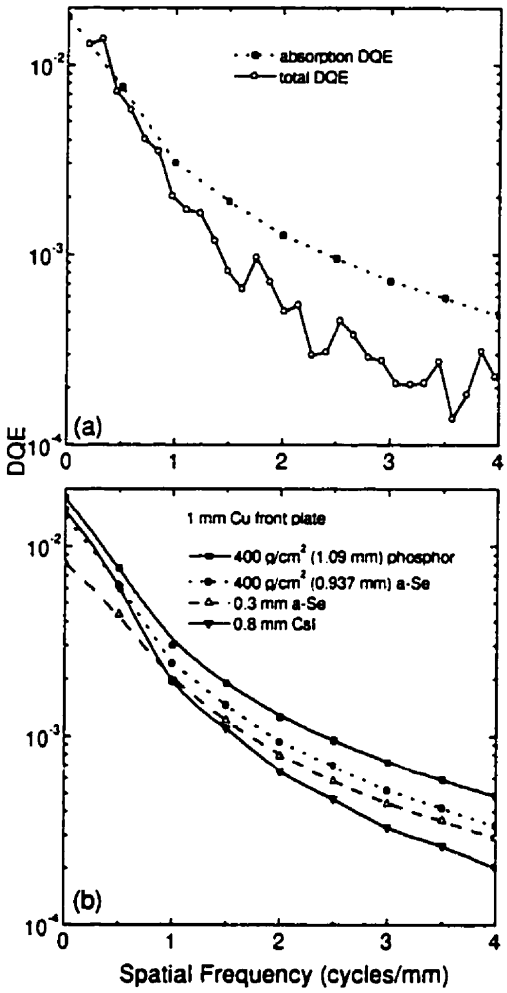

Figure 20: (a) DQE for 1 mm copper / 400 mg/cm^2 phosphor for a 6 MV entrance spectrum. Comparison is made between energy absorption DQE calculated with EGS4 and total DQE measured by Munro *et al*[29] (b) EGS4–generated energy absorption DQE with 1 mm copper plate for phosphor (400 mg/cm^2) and a-Se layers (400 mg/cm^2 and 0.3 mm)

cycle/mm. For frequencies greater than 1 cycle/mm, phosphor light production begins to affect the DQE. Although the DQE due to energy absorption can not be measured directly, the comparison to the measured DQE tends to validate the Monte Carlo calculations. For the metal/a-Se detector, the initial energy deposition process is similar to that of phosphor. However, the secondary processes such as the creation of electron-hole pairs and their subsequent migration in the electric field are not expected to change the $DQE(f)$ as drastically.

The energy absorption $DQE(f)$ of phosphor and a-Se for identical mass thicknesses are shown in Fig. 20(b). The a-Se curve lies below that of phosphor since due to the larger density of phosphor, a smaller physical thickness is needed for the same mass thickness, resulting in less spatial frequency degradation. However, since the other steps which further degrade the $DQE(f)$ are different, direct comparison of the two systems is not possible by considering only energy absorption. Results for 0.3 mm a-Se are also shown for comparison. $DQE(f)$ for another type of phosphor, CsI (0.8 mm), is also shown with a 1 mm Cu front plate.

The results for the metal/0.3 mm a-Se are shown for comparison at spatial frequencies of 0, 1 and 5 cycles/mm for increasing metal mass thickness in Fig. 21, and the $DQE(f)$ at all frequencies for different metal thicknesses in Fig. 22. As expected, $DQE(0)$ increases with metal thickness until it reaches a maximum at around d_{max}, after which

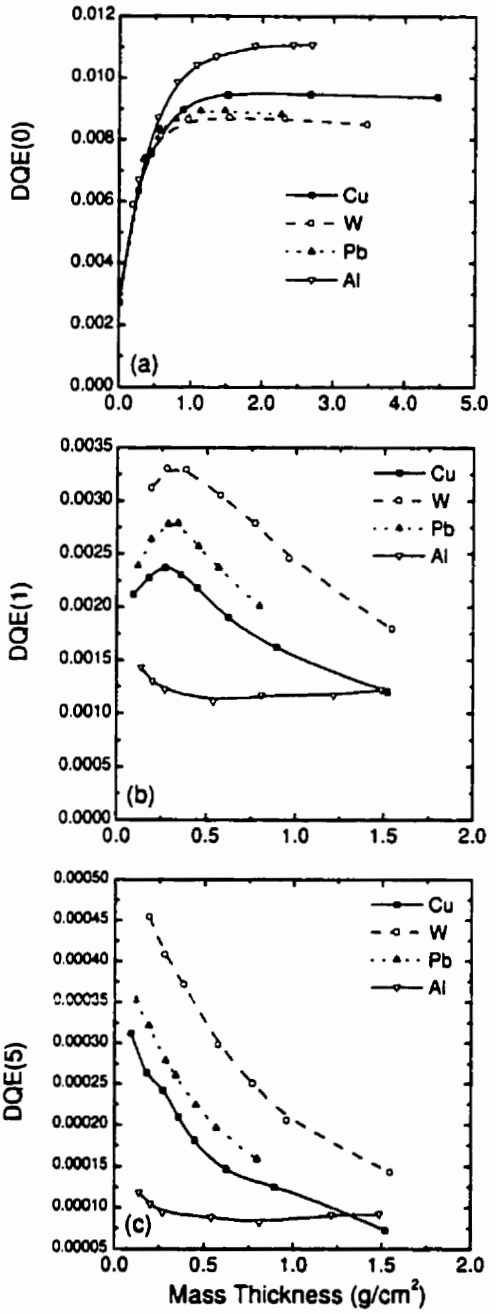

Figure 21: DQE versus metal plate mass thickness for Cu, W, Pb and Al, at three reference spatial frequencies: a) 0, b) 1 and c) 5 cycles/mm

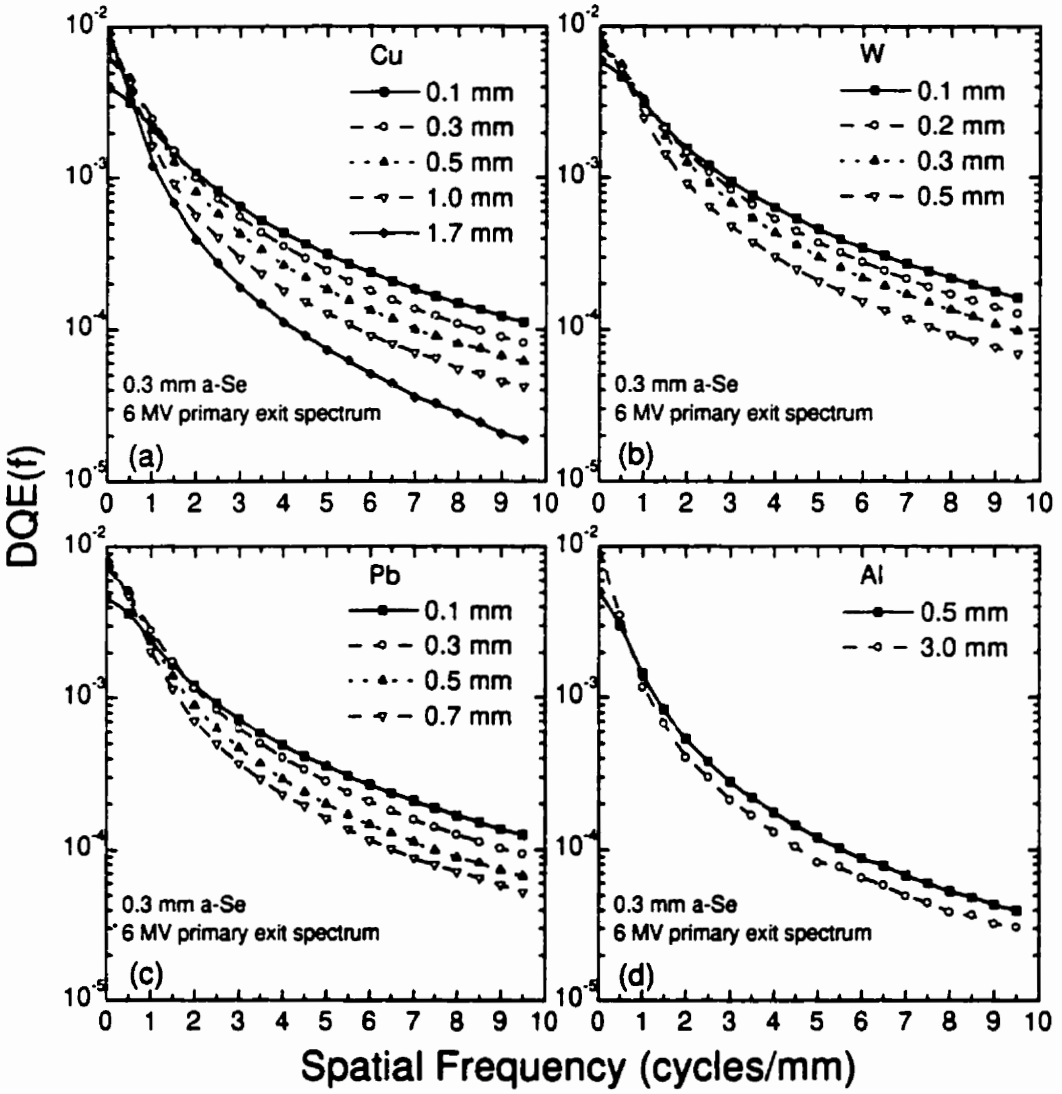

Figure 22: $DQE(f)$ due to energy absorption generated by EGS4 with 6 MV exit spectrum for different metal thicknesses. a) Cu b) W c) Pb d) Al

the $DQE(0)$ decreases. This occurs since the metal plate acts as a build-up layer, creating secondary electrons which deposit their energy in the a-Se. After a thickness greater than the maximum electron range is reached, increasing the plate thickness will only attenuate the photon beam. It should be noted that although the maximum occurs at the same mass thickness, it will occur at different physical metal thicknesses depending on the metal's density. Aluminum, which is a metal with low physical density and low atomic number attains the highest DQE at zero frequency. The reason for this warrants further study.

Comparison with $DQE(0)$ for monoenergetic photons[5] shows a degradation from approximately 0.02 for a 2.73 MeV beam to 0.009 with the exit spectrum for a 1 mm Cu front plate, which is due to increased noise originating from the incident energy distribution.

Although a thickness of d_{max} is suitable when considering zero-frequency, a cross-over occurs when DQE is considered as a function of spatial frequency f (Fig. 22). This indicates that a smaller thickness may be of more practical use, especially for viewing edges or small objects. The data can be more easily visualized in Fig. 21, where all four materials are plotted at reference spatial frequencies. If the plate thickness were chosen in such a way as to optimize for 1 cycle/mm, for example, a mass thickness of 0.25 g/cm^2 would be chosen. The effect of different spatial frequencies on portal imaging must be further investigated before an optimal plate thickness be chosen. Furthermore,

although tungsten is the worst of the four metals at zero frequency, it is the best metal plate over-all, due to its high density and smaller d_{max} resulting in improved MTF. However, not only is it difficult to deposit a-Se appropriately onto tungsten, the resultant a-Se surface on our samples is very rough. A more practical metal is stainless steel. Simulations were performed for this metal (with a composition of 70% Fe, 20% Cr and 10% Ni, and density of 8.0 g/cm^3), and were virtually identical to those of Copper.

Although the optimization of the conversion plate is the primary direction of this work, it is useful to investigate how the a-Se thickness affects the energy absorption properties of the imager. A plot of $DQE(0)$ with increasing a-Se thickness is shown in Fig. 23 for three different copper plate thicknesses. It is seen to increase approximately linearly in this range, but is obviously expected to level off and plateau at a value of unity as the thickness approaches infinity.

The full $DQE(f)$ curves for different a-Se thicknesses are shown in Fig. 24. Since the MTF decreases with increasing a-Se thickness, a cross-over occurs; however, the effect is not as great as with increasing metal thickness. This seems to indicate that when only energy absorption is considered, the largest a-Se thickness results in the highest DQE. In practice, this optimization technique would most likely not be used to determine the best a-Se thickness. Rather, contrast and latitude, which are greatly affected by the a-Se thickness, would be used as criteria.

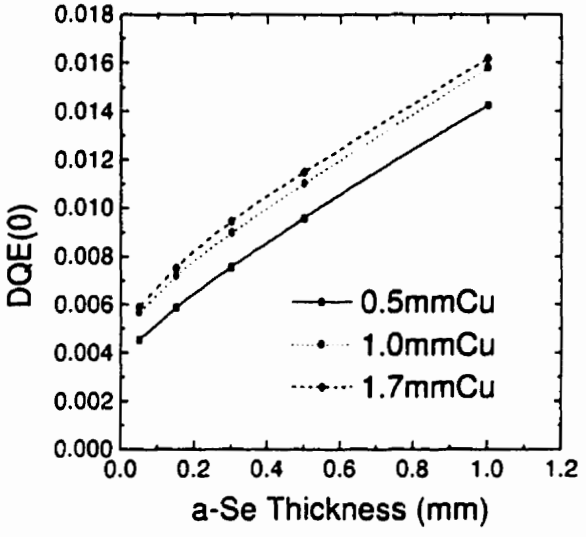

Figure 23: Zero-frequency Detective Quantum Efficiency versus increasing a-Se thickness, for three copper build-up thicknesses.

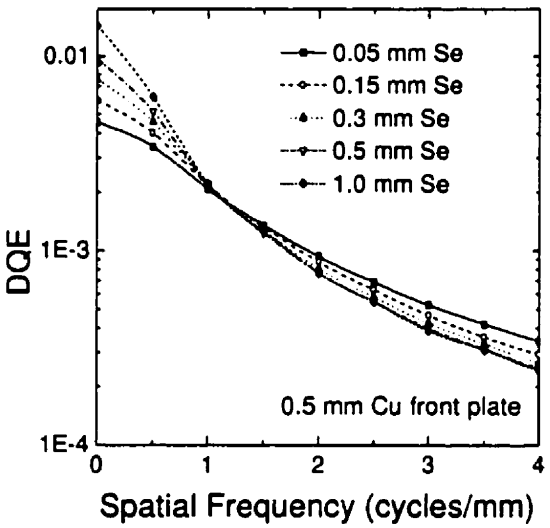

Figure 24: $DQE(f)$ generated by EGS4 for various a-Se thicknesses.

4.4 Scatter Fraction and Scatter-to-Primary Ratio

The results of SF and SPR simulations for a 20 × 20 cm^2 field are shown in Fig. 25. The SF decreases with plate thickness. This is because the plate preferentially attenuates scatter which is of lower average energy and stops electrons from the patient. As discussed in Chapter 3, the SPR is a more important parameter than SF, since it affects the patient dose needed to attain a given $DSNR$. It is also seen to decrease with metal thickness.

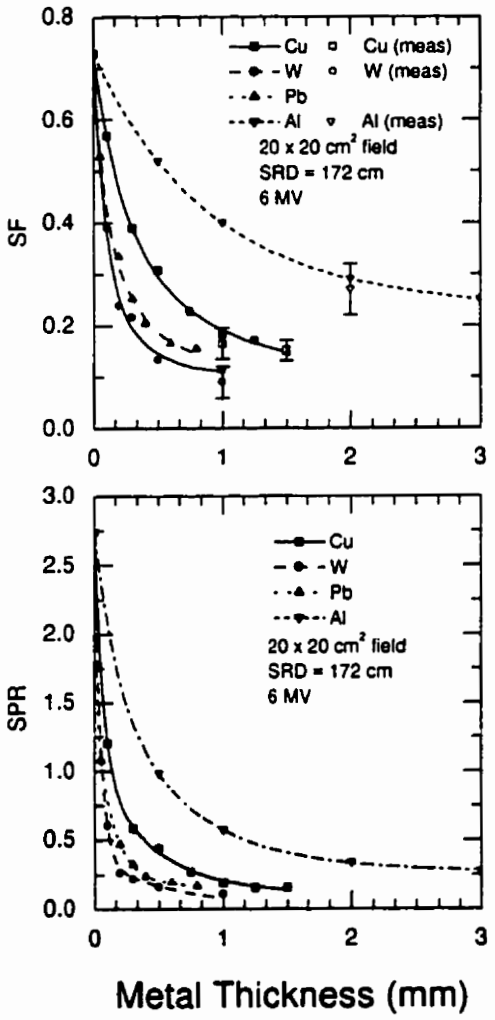

Figure 25: a) SF and b) SPR for 20 × 20 cm^2 field versus metal thickness for different metals, generated by EGS4, with a 20 cm phantom and SRD of 172 cm. Empty points (with error bars) correspond to measured values.

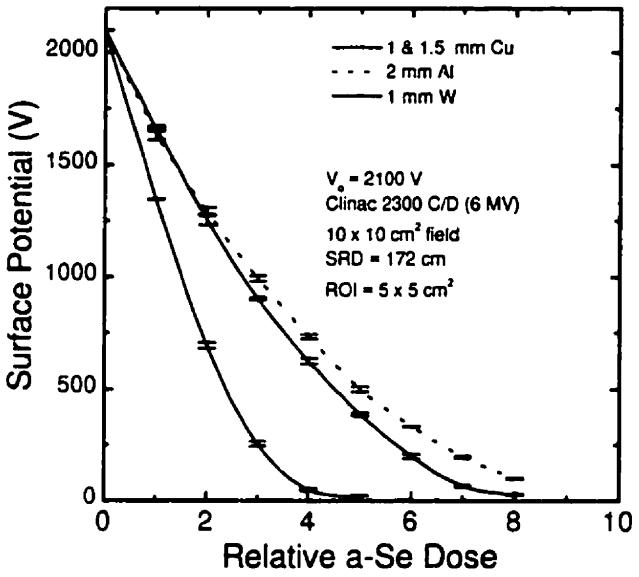

Figure 26: Measurements of Surface Potential versus Relative Absorbed Dose to a-Se, with four plates. Only one curve is shown for 1.0 mm Cu and 1.5 mm Cu plates, since they were identical within experimental uncertainties. Measured on a Clinac 2300 C/D (6 MV), SRD = 172 cm.

To measure SF, calibration curves of surface potential versus relative dose absorbed in a-Se were determined for four plates and are shown in Fig. 26. The curve for 1 mm Cu and 1.5 mm Cu were found to be the same within experimental uncertainties and therefore only one is shown to avoid clutter. It is seen that the SF curves are non-linear as expected, because the number of electron-hole pairs collected in the a-Se increases with surface potential.

The change in voltage with field size with and without a 20 cm phantom at SRD of 172 cm for the four plates was measured. The voltage was converted to relative dose by using the calibration curves described by Fig. 26. The curves of relative dose to a-Se versus field size, with and without phantom, and the corrected curve which represents the change in dose due only to phantom scatter, are shown in Fig. 27. From these the Scatter Fractions SF are calculated and are plotted for comparison with the Monte Carlo simulations in Fig. 25(a). It is seen that the measurements agree with the simulations within experimental uncertainties. The results were identical when different combinations of Monitor Units were used to expose the a-Se, as long as it was within the practical dynamic range of the plate.

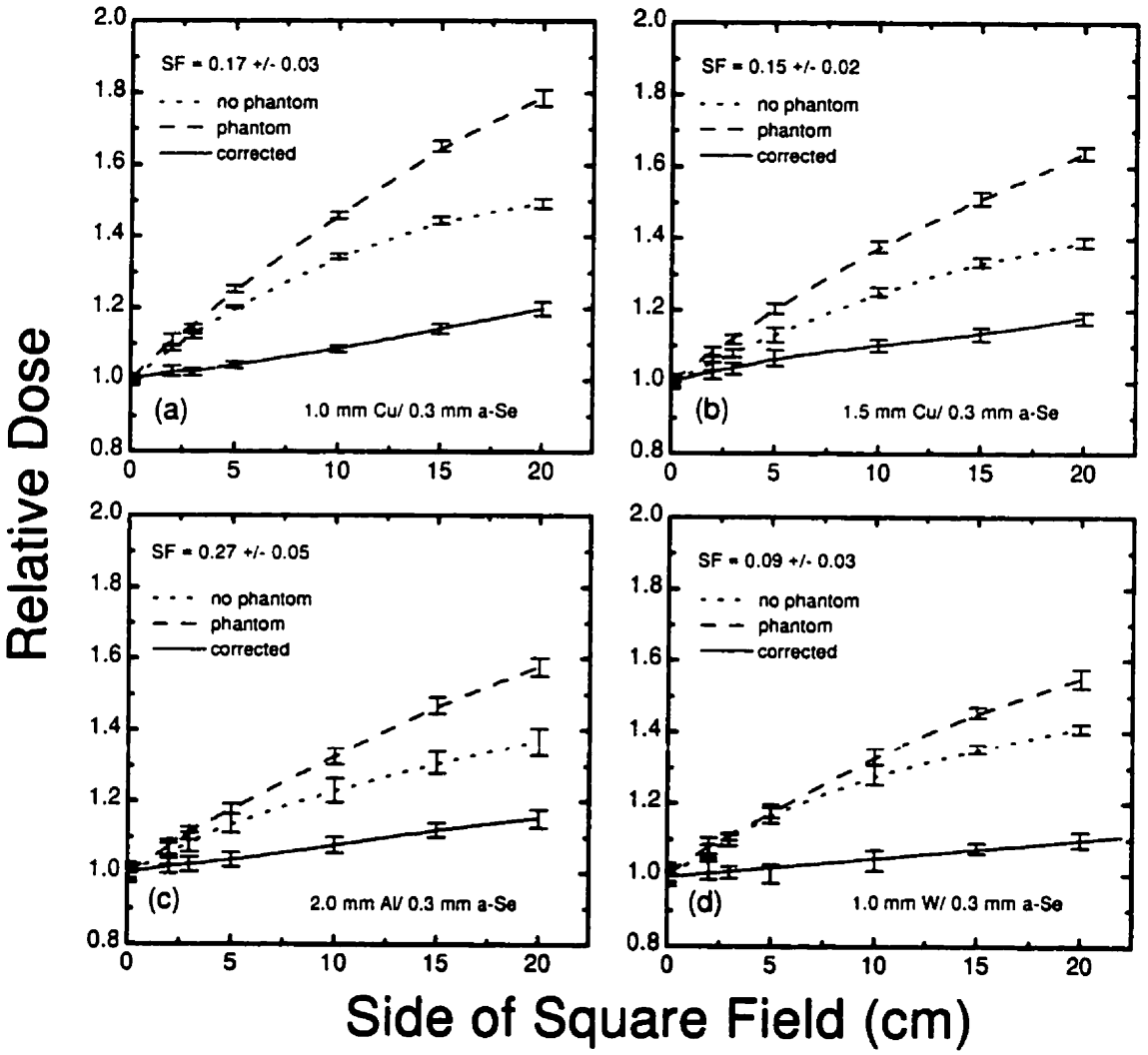

Figure 27: Measurements of relative dose to a-Se versus field size with phantom, without phantom and the corrected curve which represents the change due to patient scatter only. Measured on a Clinac 2300 C/D (6 MV), SRD = 172 cm, 20 cm polystyrene phantom.

References

[1] S. Kubsad, R. Mackie, B. Gehring, D. Misisco, B. Paliwal, M. Mehta, and T. Kinsella. Monte carlo and convolution dosimetry for stereotactic radiosurgery. *Int. J. Radiat. Oncol. Biol. Phys*, 19:1027–1035, 1990.

[2] International Commission on Radiation Units and Measurement. *ICRU REPORT 37*, 1984.

[3] P. Munro, J. A. Rawlinson, and A. Fenster. Therapy imaging: A signal-to-noise analysis of fluoroscopic imaging system for radiotherapy localization. *Med. Phys.*, 17:763–772, 1990.

[4] D. A. Jaffray, J. J. Battista, A. Fenster, and P. Munro. Monte Carlo studies of x-ray energy absorption and quantum noise in megavoltage transmission radiography. *Med. Phys.*, 22:1077–1088, 1995.

[5] H. Wang, B. G. Fallone, and T. Falco. Monte Carlo simulations of a metal/a-Se portal detector. *Radiol. Oncol*, 30:291–297, 1996.

Chapter 5: Conclusions

The $DQE(f)$, SF and SPR (for a 20 $\times$ 20 cm^2 field) due to energy absorption in a metal/a-Se portal imager have been simulated using Monte Carlo techniques as a function of metal plate thickness for four different metals using a 6 MV primary spectrum transmitted through a 20 cm polystyrene phantom. It is shown that although a thickness d_{max} is optimal for $DQE(0)$, smaller thicknesses may be better suited to optimize the response at spatial frequencies above 1 cycle/mm. Tungsten offers the best results of the four plates, but is not suitable because of the difficulty of achieving a uniform deposition of a-Se on its surface. Stainless steel offered results similar to that of Cu and is of interest because of the ease with which a-Se can be uniformly deposited on its surface.

Our Monte Carlo simulation of $DQE(f)$ is useful in optimizing the type and thickness of the front plate. However, measurements of $DQE(f)$ which incorporates the processes of the creation of electron-hole pairs and their subsequent migration in the electric field

is required to access the whole metal/a-Se detector.

Once an optimal metal plate is chosen by considerations of $DQE(f)$, the plots of SF and SPR approximate the effect of scatter on the image for a given plate thickness. Although consideration of $DQE(f)$ alone shows that smaller plate thicknesses are better for visualizing details, care must be taken to choose a thickness large enough so that scatter degradation is within acceptable limits. Scatter Fractions have been measured with our probe imager and agree with the Monte Carlo simulations to within experimental uncertainties.

With the optimization of metal/a-Se plates, the next step will be to find the most clinically useful read-out technique. The current system, which utilizes a single electrostatic probe, produces good images[19, 25, 23] but the read-out procedure is time–consuming (approximately 7 minutes to scan a 6" × 6" area). The most likely candidate will be a-Se flat panel detectors based on thin-film transistors, which offer short read-out times.

Future Work

The Detective Quantum Efficiency $DQE(f)$ of a-Se plates must be measured experimentally.

A more complete Monte Carlo model of metal/a-Se, which includes the creation and migration of electron-hole pairs, would be useful to further investigate the detector's properties. This would require experiments such as the determination of $\overline{W}$ at megavolt-

age energies to determine a recombination model. The system properties, such as MTF, could then be compared to experiment.

Investigation on the optimal image readout method to construct a clinically useful portal imager needs to be performed. The feasibility of the system for exit dosimetry must also be evaluated.

References

[1] T. Falco and B. G. Fallone. Portal imaging: Comparing metal-plate film and electrostatic-based detectors. *Med. Phys. (Abstract)*, 23:797, 1996.

[2] B. G. Fallone, T. Falco, H. Wang, and N. Araj. An electrostatic-based detector for portal imaging. *4th International Workshop on Electronic Portal Imaging, Abstract Proceedings, Edited by M. Van Herk and K. Gilhuijs, Amsterdam*, pages 64–65, 1996.

[3] T. Falco, H. Wang, and B. G. Fallone. Preliminary study of a metal/a-Se –based portal detector. *(submitted to Med. Phys.)*, 1997.

Bibliography

Note: page number where the reference is cited is found in brackets at the end of each entry

R. C. Alig and S. Bloom. *J. Appl. Phys.*, 49:3476, 1978 (p. 19).

E. Antonuk, J. Yorkston, J. Boudry, M. Longo, J. Jimenez, and R. A. Street. Development of hydrogenated amorphous silicon sensors for high energy photon radiotherapy imaging. *IEEE Transactions of Nuclear Science*, NS-37(2):165–170, 1990 (p. 5).

E. Antonuk, J. Yorkston, J. Boudry, M. Longo, and R. A. Street. Large area amorphous silicon photodiode arrays for radiotherapy and diagnostic imaging. *Nuclear Instrumentation and Method*, A310:460–464, 1989 (p. 5).

L. E.. Antonuk, J. Boudry, W. Huang, D. L. McShan, E. J. Morton, J. Yorkston, M. J. Longo, and R. Street. Demonstration of megavoltage and diagnostic x-ray imaging with hydrogenated amorphous silicon arrays. *Med. Phys.*, 19:1455–1465, 1992 (p. 5).

A. F. Biejalew, R. Mohan, and C-S. Chui. Improved bremsstrahlung photon angular sampling in the EGS4 code system. *National Research Council of Canada, Division of Physics Report*, PIRS-0203, 1989 (p. 48).

A. F. Biejalew and D. W. O. Rogers. PRESTA — the parameter reduced electron-step algorithm for electron Monte Carlo transport. *Nucl. Instrum. Methods B*,

18:165–181, 1989 (p. 30).

J. W. Boag. Xeroradiography (review). *Phys. Med. Biol.*, 18:3–37, 1973 (p. 6, 19).

A. L. Boyer, L. Antonuk, A. Fenster, M. van Herk, H. Meertens, P. Munro, L. Reinstein, and J. Wong. A review of electronic portal imaging devices (EPIDs). *Med. Phys.*, 19:1–16, 1992 (p. 3).

R. N. Bracewell. *The Fourier Transform and its Applications*. McGraw-Hill Book Company, 2nd edition edition, 1978 (p. 30).

Edited by T. R. Mackie and J. R. Palta, editors. *Teletherapy: Present and Future*. Proceedings of the 1996 Summer School. 1996 (p. 1).

C. F. Carlson. U.S. Patent 221776. 1938 (p. 6).

E.L. Cook, J. D. Edwards, O. L. Nelson, and J. E. Potts. Performance of a high resolution radiographic detector. *The society of imaging science and technology 47th annual conference ICPS*, page 699, 1994 (p. 6).

I. Crooks and B. G. Fallone. Contrast enhancement of portal images by selective histogram equalization. *Med. Phys.*, 20:199–204, 1993 (p. 3).

J. C. Dainty and R. Shaw. *Image Science*. Academic Press, London, New York, 1974 (p. 30).

R. T. Droege. A megavoltage MTF measurement technique for metal screen-film detectors. *Med. Phys.*, 6(4):272–279, 1979 (p. 3).

R. T. Droege and B. E. Bjängard. Metal screen-film detector MTF at megavoltage x-ray energies. *Med. Phys.*, 6(6):515–518, 1979 (p. 3, 14).

R. T. Droege and B. E. Bjarngard. Influence of metal screens on contrast in megavoltage x-ray imaging. *Med. Phys*, 6:487–493, 1979 (p. 2).

S. Duane, A. F. Bielajew, and D. W. O. Rogers. Use of ICRU-37/NBS collisional stopping powers on the EGS4 report. *Use of ICRU-37/NBS Collisional Stopping Powers on the EGS4 Report, PIRS-1073*, 1989 (p. 48).

T. Falco and B. G. Fallone. Portal imaging: comparing metal-plate/film with electrostatic-based detectors. *Proceedings of 42nd annual Canadian Organization of Medical Physicists Conference*, pages 56–59, 1996 (p. 7).

T. Falco and B. G. Fallone. Portal imaging: Comparing metal-plate film and electrostatic-based detectors. *Med. Phys. (Abstract)*, 23:797, 1996 (p. 7, p. 89).

T. Falco and B. G. Fallone. Characteristics of metal-plate/film detectors at therapy energies: Part 1 (MTF). *submitted to Med. Phys.*, 1997 (p. 3).

T. Falco and B. G. Fallone. Characteristics of metal-plate/film detectors at therapy energies: Part 2 (DQE). *submitted to Med. Phys.*, 1997 (p. 3).

T. Falco, H. Wang, and B. G. Fallone. Preliminary study of a metal/a-Se –based portal detector. *(submitted to Med. Phys.)*, 1997 (p. 21, 23, 91).

B. G. Fallone and T. Falco. Megavoltage imaging method using a combination of a

photoreceptor with a high energy photon converter and intensifier. *Reg. # 625063, U.S. Patent to be released in August*, 1997 (p. 7).

B. G. Fallone, T. Falco, H. Wang, and N. Araj. An electrostatic-based detector for portal imaging. *4th International Workshop on Electronic Portal Imaging, Abstract Proceedings, Edited by M. Van Herk and K. Gilhuijs, Amsterdam*, pages 64–65, 1996 (p. 7, 89).

H. F. Hare, J. Hale, and E. P. Pendergrass. Physical and clinical aspects of supervoltage rotational therapy. *Radiology*, 57:157, 1951 (p. 1).

A. Haus, J. Marks, and M. Griem. Evaluation of an automatic rapid-processable film for imaging during the complete radio-therapeutic exposure. *Radiology*, 107:697–698, 1973 (p. 2).

A. Haus, S. Pinsky, and J. Marks. A technique for imaging patient treatment area during a therapeutic radiation exposure. *Radiology*, 97:653–656, 1970 (p. 2).

M. Van Herk and H. Meertens. A digital imaging system for portal verification. *Proceedings of the 9th International Conference on the Use of Computers in Radiation Therapy*, pages 371–374, 1987 (p. 3).

M. Van Herk and H. Meertens. A matrix ionization chamber imaging device for on-line patient setup verification during radiotherapy. *Radiother. Oncol.*, 11:369–378, 1988 (p. 3).

International Commission on Radiation Units and Measurement. *ICRU REPORT 37*, 1984 (p. 73).

D. A. Jaffray, J. J. Battista, A. Fenster, and P. Munro. X-ray scatter in megavoltage transmission radiography: Physical characteristics and influence on image quality. *Med. Phys.*, 21:45–60, 1994 (p. 8, 48).

D. A. Jaffray, J. J. Battista, A. Fenster, and P. Munro. Monte Carlo studies of x-ray energy absorption and quantum noise in megavoltage transmission radiography. *Med. Phys.*, 22:1077–1088, 1995 (p. 8, 73).

H. E. Johns and J. R. Cunningham. *The Physics of Radiology*. Charles C. Thomas Publisher, 4th edition edition, 1983 (p. 16).

M. C. Kirby and P. C. Williams. Measurement possibilities using an electronic portal imaging device. *Radiother. Oncol.*, 29:237–243, 1993 (p. 2).

C. A. Klein. *J. Appl. Phys.*, 39:2029, 1968 (p. 19).

S. Kubsad, R. Mackie, B. Gehring, D. Misisco, B. Paliwal, M. Mehta, and T. Kinsella. Monte carlo and convolution dosimetry for stereotactic radiosurgery. *Int. J. Radiat. Oncol. Biol. Phys*, 19:1027–1035, 1990 (p. 44, 66–67).

J. Leong. Use of digital fluoroscopy as an on-line verification device in radiation therapy. *Phys. Med. Biol.*, 31:985–992, 1986 (p. 2).

D. Mah. *Portal Imaging with Amorphous Selenium: A signal and noise analysis and*

comparison with fluoroscopic systems. PhD thesis, University of Toronto, 1997 (p. 21).

P. Munro, J. A. Rawlinson, and A. Fenster. Therapy imaging: a signal-to-noise analysis of metal plate/film detectors. *Med. Phys.*, 14:975–984, 1987 (p. 3).

P. Munro, J. A. Rawlinson, and A. Fenster. A digital fluoroscopic imaging device for radiotherapy localization. *Proceedings of SPIE*, 321–329:1090, 1989 (p. 3).

P. Munro, J. A. Rawlinson, and A. Fenster. Therapy imaging: A signal-to-noise analysis of fluoroscopic imaging system for radiotherapy localization. *Med. Phys.*, 17:763–772, 1990 (p. 51, 73).

W. R. Nelson, H. Hirayama, and D. W. O. Rogers. The EGS4 code system. *Stanford Linear Accelerator Center Report, SLAC 265*, 1985 (p. 32, 27).

S. M. Pizer, E. P.. Amburn, J. D. Austin, R. Cromartie, A. Geselowitz, T. Greer, B. Ter Haar Romeny, J. B. Zimmerman, and K. Zuiderveld. Adaptive histogram equalization and its variations. *Comput. Vision, Graphics, and Image Processing*, 39:355–368, 1987 (p. 3).

W. Que and J. A. Rowlands. X-ray photogeneration in amorphous selenium: Geminate versus columnar recombination. *Phys. Rev. B*, 51:500–507, 1995 (p. 20).

T. Radcliffe, G. Barnea, B. Wowk, R. Rajapakshe, and S. Shalev. Monte Carlo optimization of metal/phosphor screens at megavoltage energies. *Med. Phys.*,

20:1161–1169, 1993 (p. 8).

D. W. O. Rogers and A. F. Biejalew. *The Dosimetry of Ionizing Radiation*. edited by K. R. Kase, B. E. Bjarngard, and F. H. Attix, Academic, New York, 1989 (p. 23).

D. W. O. Rogers, S. Duane, A. F. Bielajew, and W.R. Nelson. Use of ICRU-37/NBS radiative stopping powers on the EGS4 system. *National Research Council of Canada, Division of Physics Report, PIRS-0177*, 1989 (p. 48).

J. A. Rowlands, G. DeCrescenzo, and N. Araj. X-ray imaging using amorphous selenium: determination of x-ray sensitivity by pulse height spectroscopy. *Med. Phys.*, 19:1065–1069, 1992 (p. 20).

J. A. Rowlands and D. M. Hunter. X-ray imaging using amorphous selenium: Photoinduced discharge (PID) readout for digital general radiography. *Med. Phys.*, 22:1983–2005, 1995 (p. 6).

J. A. Rowlands and J. E. Taylor. Design of a laser scanner for a digital mammography system. *Med. Phys.*, 23:755–758, 1996 (p. 6).

R. Schaffert. U.S. Patent 2666144. 1950;1954 (p. 6).

S. Shalev, T. Lee, K. Lesczcynski, S. Cosby, and T. Chu. Video techniques for on-line portal imaging. *Computerized Medical Imaging and Graphics*, 13:217–226, 1989 (p. 3).

G. Sherouse, J. Rosenamn, H. McMurr, S. Pizer, and E. Chaney. Automatic degital

contrast enhancement of radiographic portal films. *Int. J. Radiat. Oncol. Biol. Phys.*, 13:801–806, 1987 (p. 3).

R. W. Swain and R. J. Steckel. Beam localization in cobalt and megavoltage therapy during treatment. *Radiology*, 86:529, 1966 (p. 2).

R. Swank. Absorption and noise in x-ray phosphors. *J. Appl. Phys*, 44:4199–4203, 1973 (p. 38).

W. Swindell, E. J. Morton, P. M. Evans, and D. G. Lewis. The design of megavoltage projection imaging systems: Some theoretical aspects. *Med. Phys.*, 18:855–866, 1991 (p. 40).

A. G. Visser, H. Huizenga, V. G. M. Althof, and B. N. Swanenburg. Performance of a prototype fluoroscopic radiotherapy imaging system. *Int. J. Radiati. Oncol. Biol. Phys.*, 18:43–50, 1990 (p. 3).

H. Wang, T. Falco, and B. G. Fallone. A metal screen-amorphous selenium based image receptor in megavoltage portal imaging. *Med. Phys. (Abstract)*, 23:1130, 1996 (p. 7).

H. Wang and B. G. Fallone. Monte Carlo calculations of the MTF and DQE of a Cu/a-Se image receptor in megavoltage portal imaging. *Proceedings of 42nd annual Canadian Organization of Medical Physicists Conference*, pages 286–289, 1996 (p. 7).

H. Wang, B. G. Fallone, and T. Falco. Monte Carlo simulations of a metal/a-Se portal detector. *Radiol. Oncol*, 30:291–297, 1996 (p. 8, 77).

S. Webb. *The Physics of Three-Dimensional Radiation Therapy*. IOP Publishing Ltd, 1993 (p. 5).

L. Wolfe, L. Kalisher, and B. Considine. Cobalt-60 treatment field verification by xeroradiography. *A. J. R.*, 18:3–37, 1973 (p. 6).

A. Zermeno, T. Kirby, R. Cowart, L. Marsh, and P. Ong. Laser readout of electrostatic images. *Application of Optical Instrumentation to Medicine VII, Proceedings of SPIE*, 173:81–87, 1979 (p. 6).

W. Zhao and J. A. Rowlands. X-ray imaging using amorphous selenium: feasibility of a flat panel self-scanned detector for digital radiology. *Med. Phys.*, 22:1595–1604, 1995 (p. 6).

IMAGE EVALUATION
TEST TARGET (QA-3)

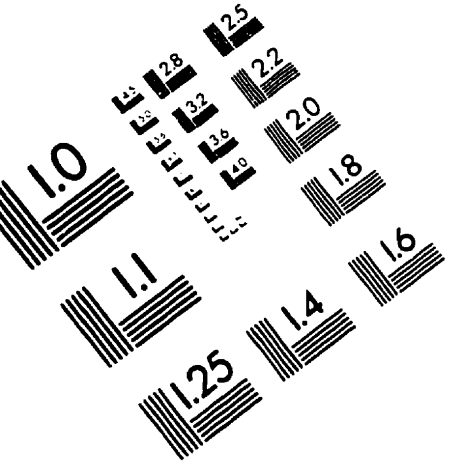

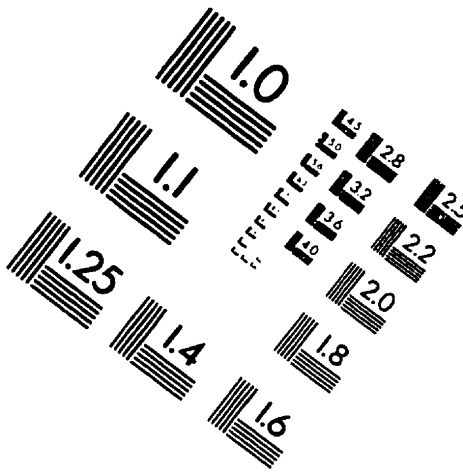

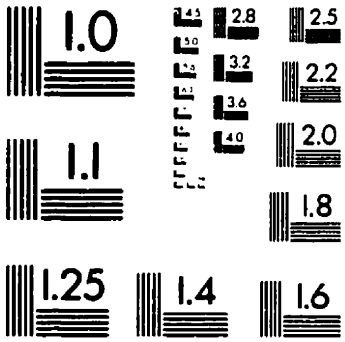

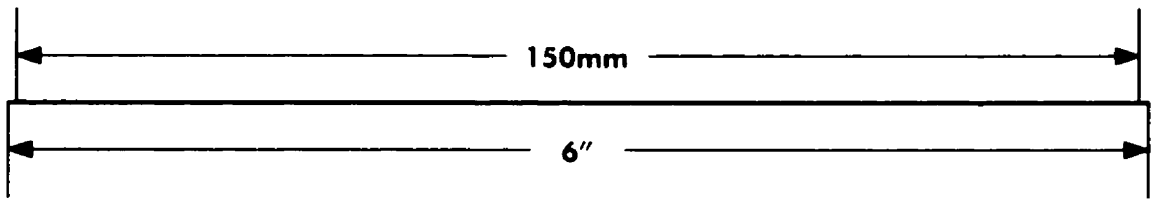

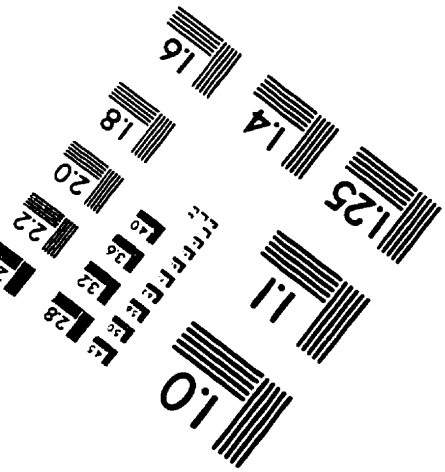

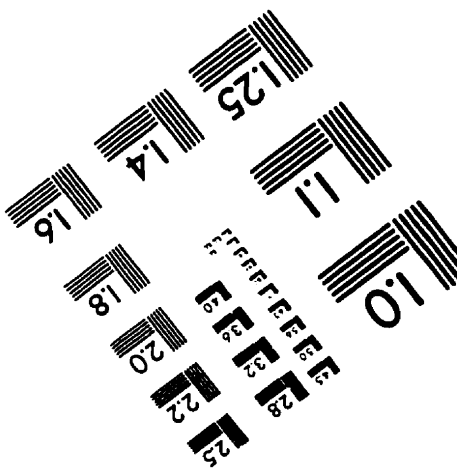

APPLIED IMAGE . Inc
1653 East Main Street
Rochester, NY 14609 USA
Phone: 716/482-0300
Fax: 716/288-5989